Centro de Investigación y de Estudios Avanzados del Instituto Politécnico Nacional

Departamento de Física Aplicada

Lambda Production at High Q^2 in Deep Inelastic Scattering Events with H1 Detector at HERA

for the degree of

Doctor of Science

DISSERTATION PRESENTED BY:

Karla Beatríz Cantún Ávila

April 2013, Mérida Yucatán

Contents

iv

List of Figures

x

List of Tables

Chapter 1

Introduction

The fist evidences for the existence of strange particles were found during 1940s. The first observation was by means of cosmic-ray studies. It was reported by Leprince-Ringuet in 1944. They observed an event in which, after a secondary cosmic-ray particle crossed the cloud chamber inmerse in a magnetic field, there were recognized a couple of curved tracks. There were possible to determine the mass of the incident particle, it was $500\pm50\ MeV$. This corresponds to the mass of the K-meson but, at that time, the particle was not identified. In 1947 Rochester and Butler, from the University of Manchester, obtained two photographs which showed the so called V-particles. These were obtained when a cloud chamber in a magnetic field and triggered by a Geiger counter detected a cosmic-ray shower. There were proposed and tested more than one hypotesis to explain the facts. Until that, there was a hypothesis which described the event as the decay of a neutral particle into a pair of oppositely-charged particles. This was found consistent with the data. After this, there were done several of similar experiments which allowed to achieve better resolution on the pattern of the data. In the mid time, due to the technique difficulties, it was not possible to check if the decaying particle and its products were coplanars, and if the conservation of the moment was fullfilled. However, the Manchester group

introduced a method to show, that two kinds of V^0-particle decay existed. The results obtained from this method, adding those obtained by R.W. Thompson and other workers established the existence of the two decays[1],

$$\Lambda \to p\pi^- \quad \text{and} \quad K^0 \to \pi^+\pi^-.$$

The study of the strange particles production provides an important tool for a deeper understanding of the strangeness quantum number, which can be used to explore the dynamic of the reaction, throught the study of the position in phase-space of a strange hadron with respect to its associated anti-strange partner, with this the momentum transfer may be study. Additionally, strange baryons enable the study of polarization effects in the hadronization process.

Chapter 2

Physics Survey

> The idea is to accelerate electrons to very high energies,
>
> then allow them to interact with a stationary proton,
>
> and investigate what happens.
>
> *(Oxford University page[3])*

2.1 ep Deep Inelastic Scattering and its Kinematics

There are two kinds of ep scattering process, *elestic* or *inelastic*. In an elastic scattering collision we may find the same number and kind of particles in the initial state and in the final state. By contrast, an inelastic sattering process is characterized by the appearance of new particles in the final state. An example of this is in the case $ep \rightarrow e'\Lambda X$. This represent, in a generic way, an *inclusive* experiment [4], which is the main purpose of this thesis. There are also a difference between ep inelastic scattering process, the *neutral current* (NC) process ($ep \rightarrow eX$) and the *charge curent* (CC) process ($ep \rightarrow \nu_e X$), these are illustrated in the Fig.(2.1). The gauge boson in the NC interactions (γ or Z^0) transforms neither charge nor mass, while in the CC interactions gauge boson ($W^{\pm}$) carries away the charge and transforms the e to an electron neutrino (ν_e). This means that the difference between these processes is given by the gauge boson who mediates the interaction, if it carries away or not the lepton charge. The framework of the present analysis concern to the NC interactions.

The kinematics of deep-inelastic ep scattering can be described by two independent

3
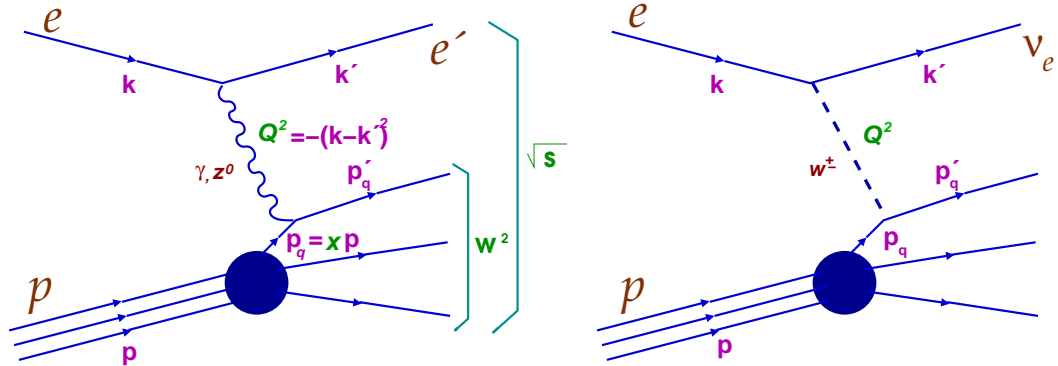
Figure 2.1: Feymann diagrams of *Neutral Current*(left) and *Charge Current*(right) *ep* scattering interactions.

variables[1], once the center of mass energy is given by energies of the incident particles. In order to describe this, we use a set of following Lorentz invariant quantities,

$$s \equiv (\mathbf{k} + \mathbf{p})^2 \approx 4E_e E_p \tag{2.1}$$

where ($\mathbf{k}$) represents the four-mometum of incoming lepton and ($\mathbf{p}$) the four-momentum of the incoming proton as is depicted at left in Fig.(2.1), E_e corresponds lepton beam energy and E_p to proton beam energy[2].

The square root of this quantity corresponds to the center-of-mass energy of the *ep* system. HERA allowed *ep* interactions with a center of mass energy $\sqrt{s} \simeq 320$ GeV. This aproximation neglects the masses of incident particles due to their large momenta, $E_e \simeq 27.6 \ GeV$ and $E_p = 920 \ GeV$.

As result of the lepton scatter, there is an transfer of four-momentum via gauge boson, the amount of this may be computed from four-mometum of incoming lepton ($\mathbf{k}$) and scattered lepton($\mathbf{k}$').

$$Q^2 = -q^2 \equiv (\mathbf{k} - \mathbf{k'})^2 \tag{2.2}$$

where the square of four-momentum transfered Q^2 is defined as the virtuality of exchanged boson.

In the infinite momentum frame the transversal impulse of quarks within the proton can be neglected[3], so the Bjorken scaling variable x represent the momentum fraction of

---

[1]If the scattering process is symmetric in the azimuthal direction, in case of it is transversely polirized there must be an additional variable to complete the description.

[2]The energy of a partice is related to its momentum and mass $E = p^2 + m^2$.

[3]The frame of reference in wich impulse of proton is very big $p^2 \gg m_p^2$, it may be described as independent partons carring a fraction of longitudinal proton momentum. This is the basis of the *Quark Parton Model* (QPM).

this carried by the struck quark[5]. It is given by:

$$x \equiv \frac{Q^2}{2\mathbf{p} \cdot \mathbf{q}} \tag{2.3}$$

this variable is an *observable* event property.

In the proton rest frame, the fraction of momentum from incident electron carried out by exchanged boson is known as *inelasticity* (y),

$$y = \frac{\mathbf{p} \cdot \mathbf{q}}{\mathbf{p} \cdot \mathbf{k}} \tag{2.4}$$

and it is constrained to take values between 0 and 1 due to four-momentum conservation as x. Neglecting electron and proton masses, these quantities are related to ep center of mass energy $\sqrt{s}$ by the equation,

$$Q^2 \simeq xys \tag{2.5}$$

which gives a maximum squared four-momentum exchange equal to center of mass energy squared, s.

The wavelength of exchange boson is related to its virtuality via $\lambda \sim \frac{1}{Q}$ [6]. From some nuclear scattering experiments it has been estimated the diameter of Proton ~ 1 fm wich correspond $Q^2 \sim 1$ GeV^2. There are two kinematics regimes distinguished according its Q^2 magnitud:

The Deep Inelastic Scattering process with Q^2 values greater than 1.

The Photoproduction process with Q^2 negligibly small.

Then as Q^2 value increase, the wavelenght associated with gauge boson are much smaller than the size of a proton, and in this sense we may say than lepton can resolve smaller structures within the proton,this is why we call *Deep* to this process (boson penetrates proton deeply).

An additional variable used to describe the kinematics of this process is the center of mass energy of boson-proton system wich is equal to the invariant mass W of the *Hadronic Final State* given by:

$$W^2 = (\mathbf{p} + \mathbf{q})^2 = ys - Q^2 + m_p^2. \tag{2.6}$$

where m_p is the proton mass. W is depicted in Fig. 2.1.

2.2   Strange Baryons Production

The strange s quark is the the third lightest quark of the elementary particle,

	Λ^0
Constituent quarks	uds
Rest mass m_{Λ^0} [MeV]	1,115.683±0.006
Iospin I	0
Total angular momentum , Parity J^P	$\frac{1}{2}^+$
Charge Q	0
Strangeness S	-1
Mean lifetime τ [s]	$2.63\pm0.020 x10^{-10}$
Decay lenght $c\tau$ [cm]	7.89

Table 2.1: Main properties of Λ^0 baryon[8].

2.2.1 Properties of Strange Hadrons

Each s quark has $S = -1$, and its associated anti-partner $S = +1$.

2.2.2 The Λ Baryon

The Lambda baryon Λ^0 is made of three quarks: u, d and s. The first time that it was observed as a neutral V^0 particle with a proton as a decay product was in 1950[7]. This discovery leads the strange quark s discovery.

In Table (2.1) are listed the specifications required to MC files used in the present work. Hereafter Λ^0 baryon is going to be refered as Λ.

6

Chapter 3

MonteCarlo Simulation

It is essentially important for an experimental analysis, and its achieves may be major, if we may test that we perform the same as theoretical models, and maybe, contribute to a better understanding of the physics involved. In high energy physics many problems may not be solved analytically, that is why stochastic description based on predictions from first principle are used to solve them. This is implemented in Monte Carlo (MC) event generators.

MC event generators are computer programs used to simulate particle collisions by means of random sampling of the possible processes, based on phenomenological models. These models can simulate the different stages and the outcome of the collision for example, $e^{\pm}p \rightarrow X$ events. Settting limits to the phase space, one may get the prediction about the value of the cross section to be obtained for a given process, for example. The MC event generator brings the possibility to combine them with detector simulations in order to investigate the detector performance and to obtain corrections for the data measured.

Once the generation process is completed, the resulted particles are processed to simulate the detector, where the particle energies and momenta are reconstructed.

3.1 Event Simulation

The MC generator models the DIS evant evolution in ep interactions in three phases in a time order:

- First the elementary scattering process is simulated based on the parton distributions used in the model and the theoretically predicted cross section.

- In a second step higer order QED and QCD radiation effects are taken into account using phenomenologycal models.
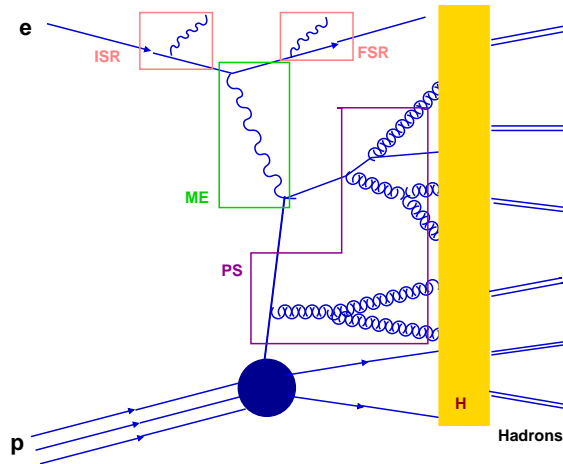
Figure 3.1: Scheme of process contributing to ep cross-section. The matrix element (ME) describing the hard scattering process, the initial and final state parton shower (PS), the initial (ISR) and final (FSR) state QED radiation and the hadronisation process (H)

- Finally in the last step, a phenomenological model takes care of the hadronisation of the partons.

The initial parton radiation is grouped with the final state radiation into the second part, even if it happens before the hard scattering process. It is because they are quite similar to each other, with the difference that the final sate radiation has backward time evolution.

In figure (3.1) is shown an scheme of the transformation from the incident beams to the final state particles, and it is divided in several part according to the physiscs that describe it.

3.1.1   The Hard Scattering Process

The hard scattering process is the core part of an interaction, it determines the main features of the event. Normally a $2 \rightarrow 2$ process is generated. In a DIS process this is $ql \rightarrow ql$. In photoproduction, for a boson-gluon fusion (BGF) process $\gamma g \rightarrow q\overline{q}$. In the case of ep process, is necessary the knowledge of the parton distribution function (PDF) of the proton in order to do it perturbatively calculable. The QED radiation may be present in a process, and could have non-negligible effects. In case of the ISR and FSR may originate a change in the event topology. Higher orders α QED effects are vertex correction and self energy.

8

3.1.2 QCD Radiation

A process with colored charge objects may have QCD radiation before or after the it. This radiation results in an iterative series of branching process like $g \rightarrow q\overline{q}$, $g \rightarrow gg$ and $q \rightarrow qg$.

MEPS There are two complementary approaches whose model the perturbative QCD radiation effects,

- The matrix element method (ME) This can calculate the Feynman diagrams order by order.
- The parton shower method (PS) This simulate the radiation by an arbitrary number of branching process.

The PS method in practice, is matched to the first order matrix elements to describe the hard gluon emission region. The ME and the PS methods are sometimes combined, depending the application. From here it is known as MEPS.

CDM Another parton shower model is the color dipol model (CDM). This considers that the parton emission comes from a color dipole between partons, instead of from single partons.

3.1.3 Hadronization

The perturbative QCD makes predictions about the final satate. To make compatible this predictions with that observed by the experiment it is necessary take into account the non-perturbative process of hadron formation. The Hadronization process only involves small momentum transfer and it is not calculable by perturvative QCD. There are phenomenological models which describe the hadronization process, the main two are the string model and the cluster model. The basic idea of them are breafly presented bellow,

The string fragmentation model start from colored objects, as quarks and gluons, and assume that a string force is formed between two of them. A tesion force is formed along the string when the colored objects begin to separate to each other, and icrease with their distance.When the string breaks, at the breaking poins a new $q\overline{q}$ or $Q\overline{Q}$ pair is created [1]. This process continues until its energy is comparavle with the energy of the final hadron.

The cluster model through the preconfinement idea, assumes that the color connected partons tend to be close to each other in the phase-space, and their combination form colorless clusters. These clusters decay to produce hadrons.

---

[1]Here $q\overline{q}$ denotes a pair of quarks and $Q\overline{Q}$ a pair of diquarks

3.2 Detector simulation

At this stage, the detector response, as close as possible to the reality, is simulated. This is done with the purpose to understand and to determine the detector effects such as the resolution, the acceptance and the presence of dead materials. All this to compensate the detector effects to the measurements in order to obtain detector independent results.

In H1, once the generation process is completed, the resulted particles are processed in H1SIM [11], a program based on GEANT to simulate the H1 detector. During this simulation, are also simulated the interactions of hadrons and leptons with the detector material and responces of subdetector electronics. In the last step the signals simulated by H1SIM are used for the reconstruction in H1REC [11], where particle energies and momenta are reconstructed from detector signals.

Simulated events from MC generators are passed through the same reconstruction algorithms as the recorded data. They are said to be on the detector level and are comparable to the reconstructed data.

3.3 Monte Carlo Programs

Djangoh The DJANGOH[12] Monte Carlo program generate simulated DIS events. The ARIADNE[13] program includes an implementation of the CDM to generate the parton showers. In this model, the struck quark and the proton remnant form a colour dipole which emits radiation in the form of gluons. The QCD cascade is simulated by the emission of gluons from colour dipoles connecting pairs of partons, correcting the first emmision to reproduce the first order matrix elements. In this approach the transverse momenta of emitted gluons are not ordering, such that CDM provides a BFKL-like approach.

The DJANGOH program, with QCD cascades produced by ARIADNE, has been used as the default choice of Monte Carlo generator in this analysis. The predictions of Djangoh are also labeled as CDM in the figures.

Rapgap The RAPGAP[16] Monte Carlo program matches first order QCD matrix elements to DGLAP based leading-log parton showers (MEPS) with k_T ordering for the simulation of DIS events. The hard matrix elements include BGF and QCD Compton scattering processes for γ^* and Z^0 exchange.

In figure (3.2) is shown, at left, a scheme of the parton emission as considered by Django, and at right, as considered by RAPGAP.

The hard partonic process has been generated at Born level and at leading order in α_s, convoluted with PDF for the proton, which are set to be CTEQ6L[17]. To perform the hadronization both models use the LUND[18] string fragmentation algorithm to obtain the complete hadronic final state from the shower of partons generated in the previous stage.

10
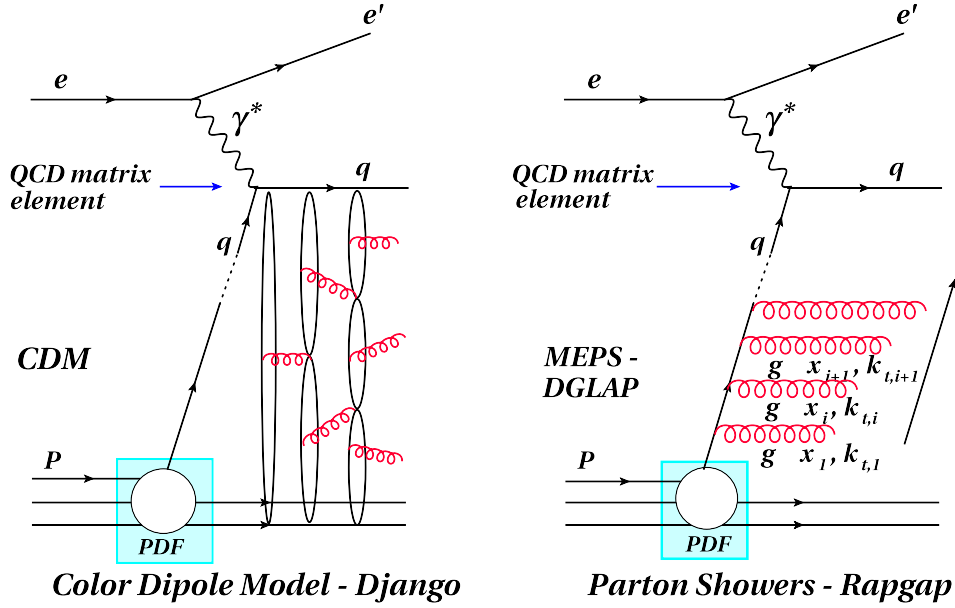
Figure 3.2: Schemes of the parton emission as considered by Django (at left) and Rapgap (at right).

In the case of DJANGOH/ARIADNE it is implemented in the JETSET[19] program. In the case of RAPGAP it is implemented in PYTHIA. This programs are interfaced with HERACLES [20], which generates NC DIS events and provides the electroweak radiative corrections.

Due to the various approximations and models implemented in MC programs, there is a number of free parameters to be tuned. Some of them are related with the hadronization stage, which, in spite of to be assumed as independent of the model used to obtain the partonic final state, some of its parameters are sensitive to the specific implementation of the parton shower and hadronization. Then, they must to be adjusted individually. Some of these parameters are related with the strangness production. The values of them are set to the default value during the simulation.

Both PYTHIA and JETSET allows that u, d, and s quarks can be produced with some arbitrary suppresion factor. The relative strange suppression factor λ_s is which determine the relative production with respect to light u and d quarks in the string model. Other parameters related with the baryon production are: the diquark suppression factor λ_{qq} is related with the probablity of obtaining a light diquark pair $qq\overline{qq}$ from the vacuum with respect too a light quark $q\overline{q}$ pair, and the strange diquark production suppression factor λ_{sq} which models the relative production of strange diquark pair. These parameters are

defined as:

$$\lambda_s = P(s)/P(q) \qquad \lambda_{qq} = P(qq)/P(q) \qquad \lambda_{sq} = (P(sq)/P(qq))/\lambda_s \qquad (3.1)$$

The default values used for the simulation of hadronization are the tuned to hadron production measurements by ALEPH collaboration[22]:

$$\lambda_s = 0.286 \qquad \lambda_{qq} = 0.108 \qquad \lambda_{sq} = 0.690 \qquad (3.2)$$

Only λ_s has taken two different values in the present work for comparison of the predictions.

In Table (3.1) are listed the specifications required to MC files used in the present work.

MC files
PDF for proton: CTEQ6L
ALEPH tuning
$Q^2 > 60\ GeV^2$
Weights: Lumi, Zvtx, NCQCD, NCTrig, NCVtxTrackWeight

Table 3.1: Requirements of the MC files to be used in the present analysis.

Chapter 4

Experimental Survey

The physics data used in this thesis were collected by the H1 Detector, one of the two *collider experiments* at the *ep* collider **H**adron **E**lektron **R**ing **A**nlage (HERA) at **D**eutsches **E**lektronen **S**ynchrotron (DESY) in the western suburbs of Hamburg, Germany.

4.1 The HERA *ep* Collider

The HERA facility was built from 1984 to 1992, year in which started operation and continued, with various short breaks until August 2000. Then after a long break necesary to upgrade the accelerator and detectors, restarted operations in the Autumn of 2003, and was stopped at mid 2007. HERA was the unique high-energy collider which provided electron[1]-proton collision at center of mass energy above 300 GeV. Since it started until 2000, HERA provided collisions between 27.5 GeV electrons and 820 GeV protons, and by convention, this period is refered to as HERA I. After the upgrade done during the 2000/2001 shutdown, the electron beam was tuned to be polarized longitudinally and the proton energy achieved was 920 GeV, this physics data-taking period is called HERA II [2].

HERA consisted of two storage ring, allocated 15-30 m. underground in a circumpherence tunel 6,300 m long with four curved sections and four straight sections where the experimental halls located, as may be seen in figure (4.1). Each curved section has a radius of curvature of 797m.

The HERA particle beams were delivered in so-called *bunches* with 96ns bunch crossing intervals, some of HERA desing parameters are shown in Table (4.1).

---

[1]Hereafter, both electron and positrons are refered to as electrons, unless explicitly stated otherwise.

[2]Hereafter this data-taking period is going to be refered to as HERA instead of HERA II, due to the data-taking period being considered (2004-2007) in this analysis, which corresponds to HERA II.
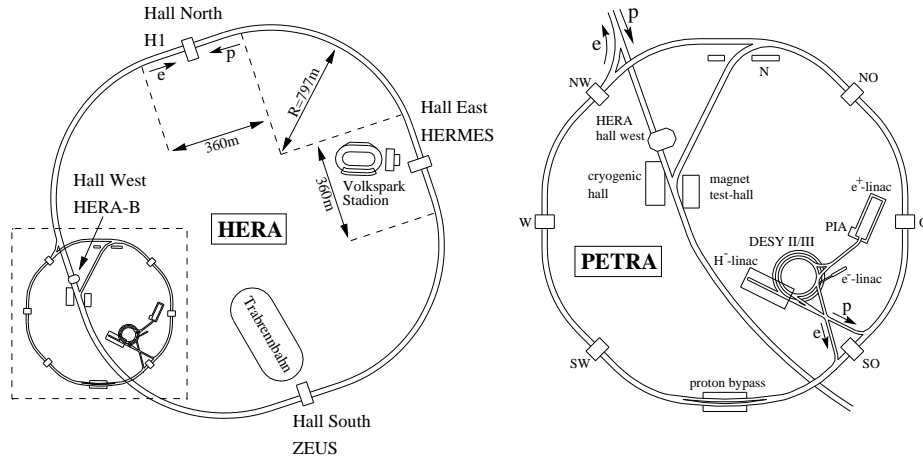
Figure 4.1: HERA Collider

Parameter	p Ring	e Ring
Tunnel lenght	6336 m	
Beam energy	920 GeV	27 GeV
Total current	110 mA	45 mA
Magnetic Field	4.65 T	0.165 T
Bunch number per ring	210	
Bunch lenght	11 cm	0.8 cm
Stream of beam	163 mA	58 mA
Collision frequency	10.4 MHz	
Luminosity	1.5 X $10^3 \frac{cm^2}{s}$	

Table 4.1: HERA design parameters

There were two big detectors, located at North Hall (H1 experiment) and South Hall (Zeus experiment), around the interaction regions where particle beams were collided, to observe the products of such collisions.

At East Hall the HERMES experiment investigate the quark-gluon structure of matter, i.e. the spin structure of the nucleon, by colliding the electron beam with a fixed target. And at the West Hall the HERA-B experiment studies the CP violation in the decay of B-mesons, by using collisions of protons with the nuclei of target wires positioned in the halo of the HERA proton beam.

The electron and proton beams were accelerated independently. The electrons were first accelerated in Linear Accelerator to 220 MeV [3], and then, they were injected to the DESY II synchrotron to be accelerated up to 7.5 GeV. From there they were passed to PETRA II with up to 70 bunches spread by periods of 96 ns and then accelerated to the

---

[3]Positrons were first accelerated to 450 MeV
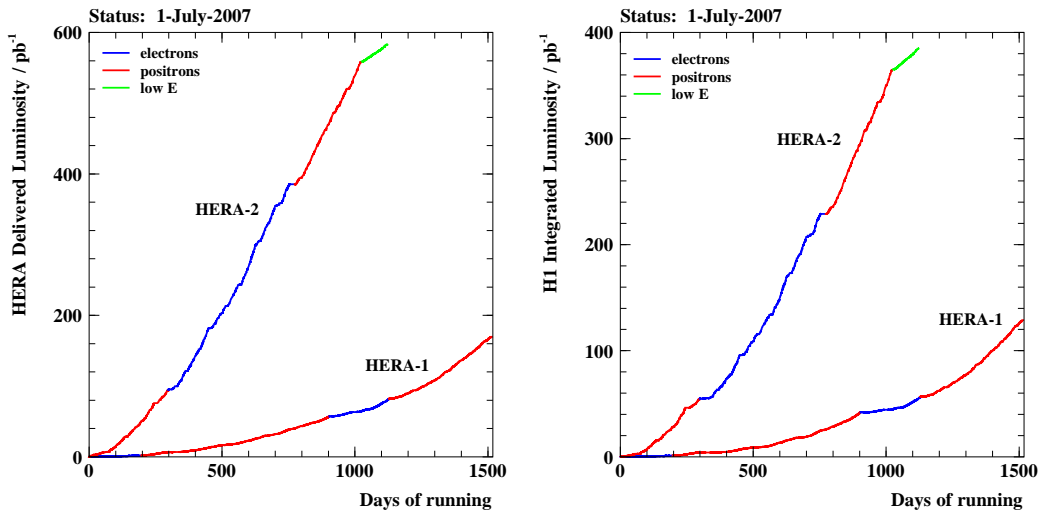
Figure 4.2: Integrated luminosity produced by HERA during the data taking period HERA II at left, and the corresponding to integrated luminosity accumulated by H1 at right

HERA injection energy of 14 GeV to be accelerated in HERA to 27.52 GeV. For the difraction of the electron beam, a magnetic field of 0.165 T was needed in the ring, which was provided by electromagnets. The energy of electrons in circular accelerators is limited by synchrotron radiation, in HERA this amount was 127 MeV per circulation. Electron beams were used originally but they were swiched to positrons due to positron beams having a longer lifetime. Positrons repel the positive ions remaining in the beam pipe, on the other hand, electrons attract such ions and with this, they increase their interaction rate, which shortens their lifetime.

For their part, protons, which began as H^- ions, were accelerated in a Linear Accelerator to 50 MeV in order to be injected to DESY III synchrotron. The electrons are removed by passing the ions through a thin foil, and then the remaining protons are accelerated to 7.5 GeV forming 11 bunches spread by periods of 96 ns. Then, they are injected to PETRA to be accelerated to 40 GeV. To achieve the proton beam diffraction super-conducting dipole magnets were used, which provided a magnetic field of 4.7 T.

A typical run may contain a maximum of 210 bunches, of which there were tipically, ~174 colliding bunches, ~15 unpaired electron bunches , ~6 unpaired proton bunches and ~15 empty bunches. The unpaired bunches, also called *pilot bunches*, and empty bunches were used for background calibration purposes.

15

4.2 The H1 Detector

A composite detector uses particles generated from interactions to measure their energy and position, in order to achieve the objective of reconstructing the physics event. The H1 detector is a multipurpose device designed to study various aspects of ep scattering. It was built in the late eighties, their dimensions were $12 \times 10 \times 15$ m^3 with an approximately 2800 tons weight. The H1 detector was designed to be cyllindrically symmetric around the beam axis, but due to the highly asymmetric energy between incoming beams, it was designed to had more elements in the outgoing proton direction, refered to as *forward* region than in the incoming proton direction, refered to as *backward* region. The region around the interaction point (IP) is called the *central* region. An schemmatic view of the H1 Detector is presented in fig (4.3).

The H1 detector used a right-handed Cartesian coordinate system with origin at the nominal ep IP, the direction of the incident proton beam defines the positive z direction, the y direction goes up-wards and the x direction points to the center of the HERA ring. In spherical coordinates (r, θ, ϕ), the polar angle θ is defined from the positive z direction and the azimuthal angle ϕ from the positive x axis, as illustrated in fig (4.4). The pseudorapidity η, defined as $\eta = -ln(tan\theta/2)$, is more useful than polar angle because it transforms nearly additively under boosts along the z direction.

According to their purposes each subdetector may be grouped in different systems. In general terms they were: the tracking detectors, the calorimeters, the muon system and the luminosity system. To support all the hardware measurements, there was the software system known as: the trigger system.

Inthe following sections we give a brief description of the subdetectors directly involved in the adquisition of the data used in our analysis. A full description of H1 detector can be found in [24, 25].

4.2.1 Track Detectors

The H1 Tracking system was designed to provide triggering, reconstruction and momentum measurement of charged particle tracks. The tracking system was divided in two main components: the Central Tracker Detector (CTD), which covered the polar range $15° < \theta < 165°$, and the Forward tracker Detector (FTD), which covered $7° < \theta < 25°$. Both consisted of drift and multi-wire proportional chambers (MWPC), see Table (4.2.1)

The CTD is composed of various concentrical subdetectors as shown in figure (4.5), two Central Jet Chambers (CJC1 and CJC2), the Central Outer Proportional chamber (COP), the Central Outer z-Chamber (COZ), the Central Inner Proportional chamber (CIP), the Central Silicon Tracker (CST).

CST is the innermost subdetector of H1. The CST consists of 32 sensors ladders with 192 sensors surrounding the beam pipe. This sillicon tracker detector, with an elliptical

THE H1 DETECTOR

Forward Muon System

Central Muon System

Forward Tracker

Central Tracker

Silicon Tracker

Veto　　**Lumi**

Had Spacal

Backward DC

PLUG TOF　　　**LAr Calorimeter**　　　**EM Spacal**
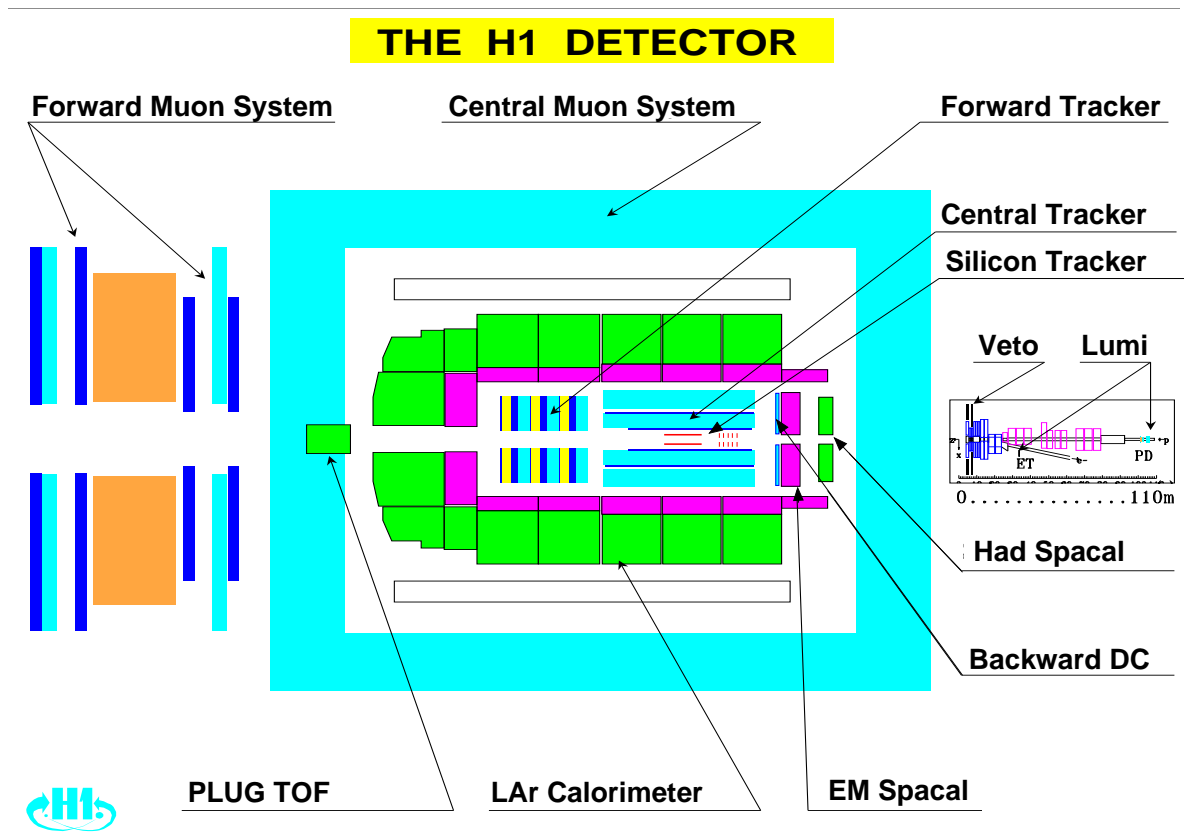
Figure 4.3: Schematic view of the H1 detector
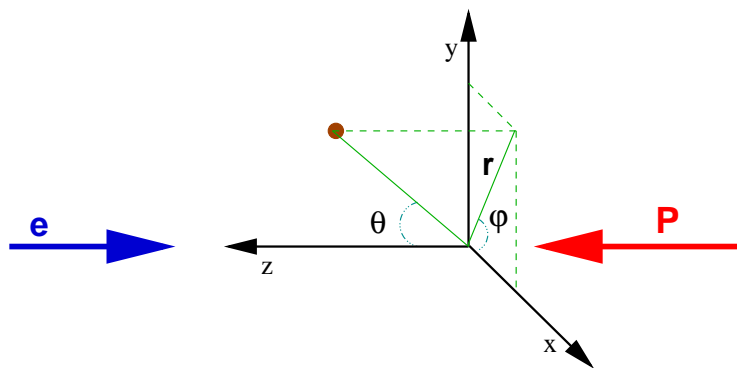
Figure 4.4: Ilustration of H1 coordinate system.

17
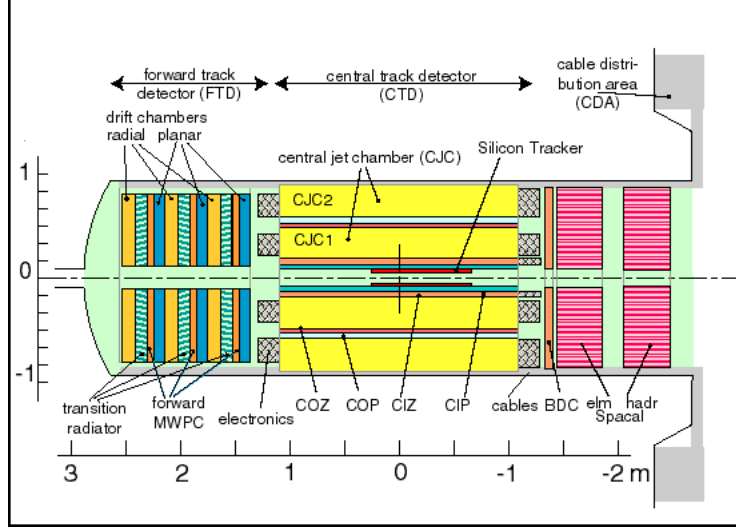
Figure 4.5: Side view of the H1 Tracker Detectors system. The Central Inner z-Chamber (CIZ) was removed to leave space for the Central Inner Proportional Chamber (CIP) used in the HERA II period of running.

cross section, has sensor strips parallel to $z - axis$ on the the inner layer with 12 ladders and the outer layer with 20 ladders [26]. The hit resolution is $\sigma_{r\phi} = 12\mu m$ and $\sigma_z = 22\mu m$.

CIP is a Multiwire Proportional Chamber (MWPC) which consists of 5 separate layers. It is used to provide trigger signals.

The Drift Cambers CJC1 and CJC2 are the most important subdetector of the tracker system. They are placed in a 1.15T magnetic field paralel to z-axis. Therefore, charged particles go through it following an helicoidal trajectory, which projected onto the $r\phi$-plane provide a circle with a radius inversely proportional to the transverse momentum of the particle. The sensor wires which comform these chambers supply a signal induced by charged particles which allow to reconstruct the *hit*. CJC1 is composed of 720 sensor wires distributed in 30 azimuthal cells by 24 radial layers

	Central Tracker System	
Range coverage	$15° < \theta < 165°$	$150 < r < 850mm$
	Forward Tracker System	
Range coverage	$7° < \theta < 25°$	$120 < r < 800mm$

Table 4.2: H1 track detectors system design parameters

18

each one. CJC2 is composed of 1920 sensor wires distributed in 60 azimuthal cells by 32 radial layers. Thus it has a spacial resolution of $\sigma_{r\phi} = 170\mu m$ and $\sigma_z = 2.2cm$.

COZ is used for the precise measurement of the z coordinate of charged particle tracks. The chamber has a cylindrical shape divided in 24 rings of 9 cm wide each and covers the polar angle range $25° < \theta < 125°$. The COZ rings have sense wires strung perpendicular to the beam line.

4.2.2 Calorimeters

In particle physics, a calorimeter is an apparatus designed to measure the energy of particles emerging from a collision. After the collision, the emerging particles generate cascades of interactions with the diferent subdetectors located around. During this process most of the energy of the particles from showers entering the calorimeter, is deposited on it. Atomic exitation or ionization are some of the characteristics of the interactions with matter used to generate a detectable effect, via particle charges. Calorimetry is the only practicable way to measure neutral particles produced in a high-energy collision. There are different types of calorimeters, the electromagnetic calorimeter designed to measure the energy of particles that interact primarily via the electromagnetic interaction, and the hadronic calorimeter designed to measure energy of those interacting via the strong nuclear force.

In H1 detector there were four different calorimeters: Liquid Argon Calorimeter (LAr) covering central and forward regions, Cooper-silicon Calorimeter (PLUG) covering the very foward regions ($0.6^o < \theta < 3.5^o$), Backward Calorimeter (SPACAL) covering the backward region, and the Hadron Calorimeter (TC) which detects the energy leakage through the LAr, important for jets with energies above 120 GeV. The main calorimeter most directly involved with our data was the first one.

Liquid Argon Calorimeter

The calorimetric measurement in the central and forward direction in the H1 detector is provided by the Liquid Argon calorimeter (LAr), which covers an angular range between $4^o < \theta < 154^o$. This calorimeter consists of an active medium, an ionizing noble liquid, which generates the signal (liquid Ar) and a passive medium which functions as absorber or converter material, the inner part uses lead absorbers to detect the electromagnetic showers (electromagnetic section, ECAL), whilst the outer part is equipped with steel absorbers to detectt hadronic showers (hadronic section, HCAL). Liquid Argon (LAr) technique possesses some properties relevant for calorimetry, such as a long-term stability and easy of calibration, fine granularity for e/π separation and energy flow measurements as well as homogenneity of response. The charge collection time is quite long (100ns), and acceptable signal-to-noise ratios with short shaping times can be obtained [27].
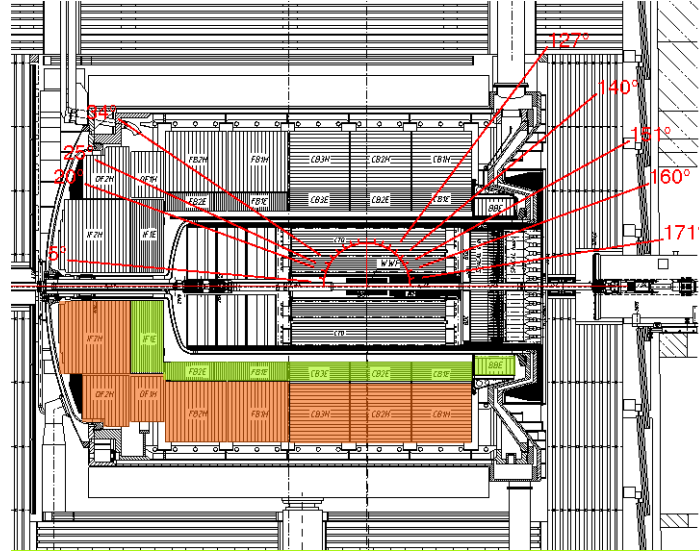
Figure 4.6: $r - z$ view of the liquid Argon calorimeter. LAr is divided into eight wheels labeled according to its position with respect the interaction point (WWP) either central (CB), backward (B) or forward (FB,IF,OF)Those modules which corresponds to the electromagnetic or hadronic section are in addition labeled with E(in green) or H(in orange) respectively.

The LAr cryostat temperature is 90 K, it is located inside a superconducting solenoid coil to minimise the amount of dead material in front of the calorimeter. Its total thickness varies between 4 to 8 interaction lengths(λ). The LAr calorimeter is divided into eight wheels in the z-direction (See fig (4.6)): Backward Barrel Electromagnetic calorimeter (BBE), Central Barrel calorimeter modules (CB1,CB2,CB3), Forward Barrel calorimeter (FB1,FB2), Outer and Inner calorimeters (OF,IF). In the radial direction, six of eight calorimeters listed above are composed of ECAL and HCAL parts, the BBE calorimeter consist of only one ECAL part and OF is conformed by two HCAL parts. Each wheel is divided into eight octants in the azimutal angle ϕ.

To obtain a uniform energy resolution, the orientation of the plates is arranged such that the angle of incidence of particles coming from the interaction point is always larger than 45°. The energy resolution of the electromagnetic part of the calorimeter is $\sigma_E/E \approx 11\%/\sqrt{E/GeV} \oplus 1\%$ while the hadronic part has an energy resolution of $\sigma_E/E \approx 50\%/\sqrt{E/GeV} \oplus 2\%$

The LAr is equipped with a trigger system which sums the energy deposits in certain regions of the calorimeter and compares them with thresholds.
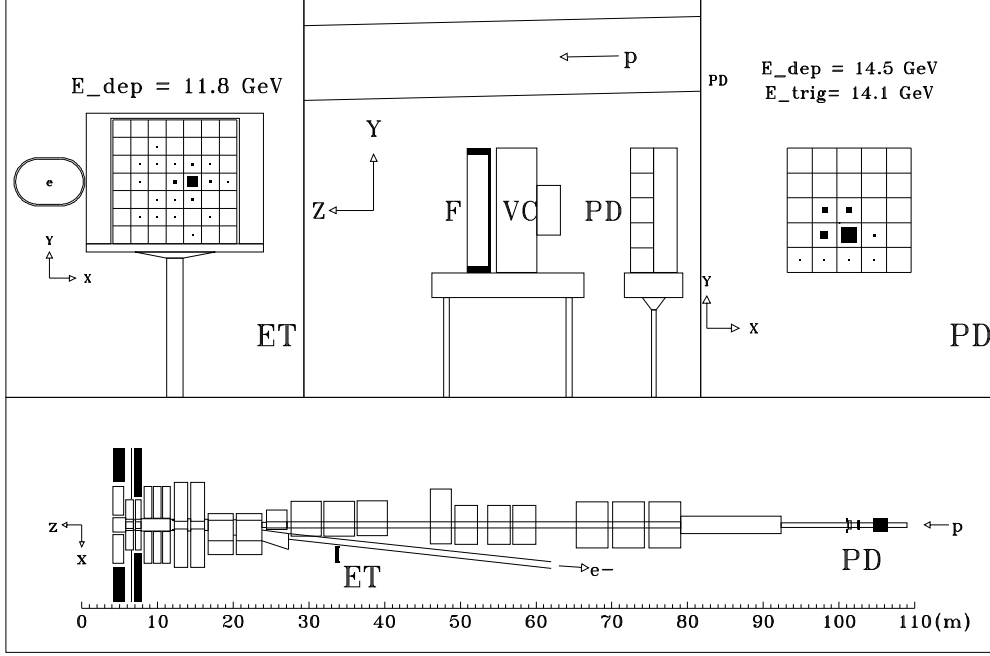
Figure 4.7: The Luminosisty system. The ET is placed at -33.4 *m*, PD is at -102.9 *m*

4.2.3 The H1 Luminosity System

The accurate determination of the luminosity delivered to the H1 experiment is absolutely necessary to compute the cross section. To monitor the luminosity, the rate of the Bethe-Heitler reaction $ep \rightarrow ep\gamma$ is measured.

The luminosity system in our experiment consists of two main subdetectors, the electron tagger (ET) and the photon detector (PD), which, due to the very small angular separation between the electron and the photon ($\sim 16\mu rad$), are placed far away from the H1 interaction point in the electron direction in the acceleration tunel. See fig (4.7). The ET is located at -33.4 *m* and the PD at -102.9 *m*.

The sum of the outgoing e and γ energies is constrained, in the limit $Q^2 \rightarrow 0$, to the electron beam energy, i.e. $E_e = E_{e'} + E_\gamma$. A threshold is applied at 5 *GeV* to both energies to remove noise and trigger threshold effects. The electron detector detects electrons with an energy fraction between 0.2 and 0.8 with respects to the beam energy and angles ($180° - \theta \leq 5$ *mrad*) and is also used as a trigger in photoproduction interactions. The ET consist of 49 crystal calorimeters read out by photomultipliers. The PD consist of 25 crystal of the same design as ET. A lead filter (F), placed in front of the photon detector, protects it from the high synchrotron radiation flux, and just behind F, a Cherenkov Veto Counter (VC) is mounted to reject events with photons originating from interactions in the filter.

21

4.2.4   The H1 Trigger System

As we mentioned before, the HERA particle beams are delivered as bunches crossing each $96ns$, which corresponds to the very high beam crossing frequency of 10.4 MHz, but interactions are dominated by background events. The genuine ep interactions which may provide us with interesting physics events are present at a much lower rate. The main purpouse of the trigger is to minimize the dead-time of the experiment, which is the time following a trigger in which the signals from the subsystems are being read and therefore the subsystems are insensitive to new events. Due to hardware and cost limitations, a very accurate trigger system is required to reduce that collision rate to ~ 10 Hz, which is the maximal rate achieved to store the events permanently. The H1 trigger system is organized in several succesive stages, denoted L1 to L4, with increasing decision times.

Level 1 (Decision time 2.3 μs): This stage consist of nine different trigger systems, each based on the information given by a subdetector. Each subdetector stores its data in a pipe-line with a depth of 22 bunch crossings. The outputs of these systems are called trigger elements (TE), i.e. $\{yes/no\}$ decisions encoded in bits. Trigger bits are sent to the Central Trigger Logic (CTL), which calculates logical combinations. The types of information from which TE are created include:

Calorimeter energy: signals in LAr and SPACAL are summed in towers and compared to thresholds in order to find jet and electron candidates. In LAr there are defined 14 Big Towers (BTs) in θ and 16 in ϕ, these are sectors where we obtain a digitalized signal which is the sum several analog signals converted that comes from a group of trigger towers (TT).

Z-vertex: information from central tracker MWPCs which is used to determine the position of the interaction vertex.

Time-of-flight: the ToF systems are used to generate triggers for in-time events or veto for background events.

Muon tracks: the central muons system generates triggers for muon in iron return yoke. The forward muon system information is processed by a sophisticated trigger system which extracts a t_0 and pointing track candidates from the drift chambers signals.

TEs then combined into so called subtriggers (ST). Up to 128 STs can be defined in order to select interesting physics events (physics triggers), to monitor detection efficiency (monitor triggers) or to select cosmics ray events for calibration purposes (cosmic triggers). The rate of each subtrigger is computed separately and can be prescaled if needed. Once a trigger condition is fulfilled ($L1\_KEEP$) the pipe-lines are frozen. Dead time starts to accumulate. This first stage requires a decision after $2.3\mu s$, which is the time limit given by the depth of the pipe-lines. The subtrigger used in this analysis is $S67$ which corresponds to the group of the LAr-based TEs.

Restart of data taking

1 B.C.=96ns   ~10MHz

Stop

Trigger data

Subdetector data

L1-reject

L1 2,3 µ s   (Pipeline)
Hard wired logic

max.1kHz

L2-reject

L2 20 µ s
Neuronal network
Topological trigger

Start

max.200Hz

L3-reject

L3 800 µ s
Microprocessor

Aborting

max.50Hz

L4-reject

asynchroner Ereignis-Puffer

L4 100 ms
RISC Processor farm

~10 Hz

Monitorevents

Rawdata on tape
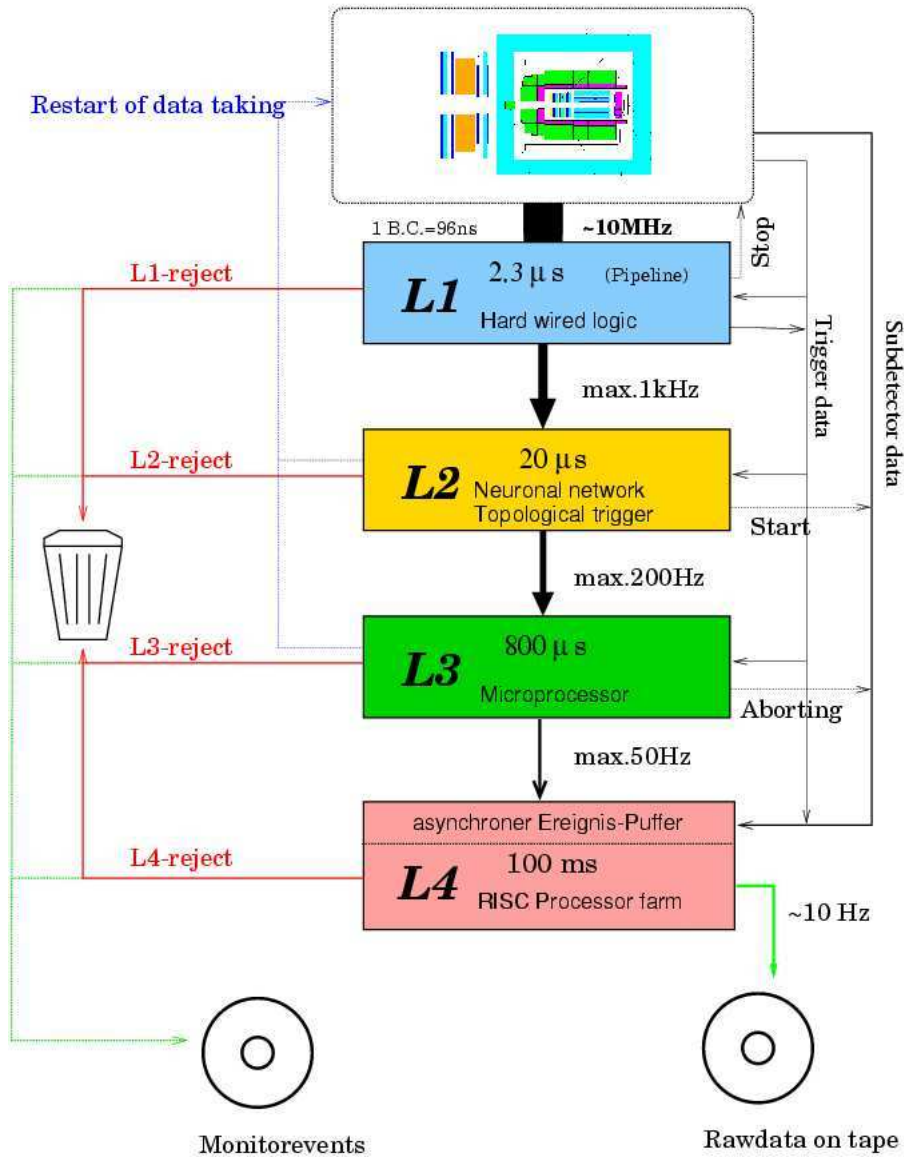
Figure 4.8: The H1 Trigger system. Schematic view of trigger levels.

Level 2 (Decision time 20 μs): Once the event is accepted on level 1 a more complex analysis of the event candidate is performed. Selection criteria are derived from special topological patterns (L2TT) or the response of neural networks (L2NN). A level 2 decision has to arrive within 20 μs. If an event is rejected ($L2\_REJECT$) the pipe-lines are immediatly enabled again, otherwise the pipe-lines are read out.

Level 3 (Decision time 100 μs - 800 μs): This trigger level is based on software filters running on commercial processor boards. L3 was installed as a part of Fast Track Trigger (FTT) and was in operation since 2006 summer. FTT utilises 12 wire layers out of the 56 wire layers of the H1 Central Jet Chambers. These wires, organized in four groups, search for track segments.

Level 4 (Decision time 100 ms): Integrated in the central data adquisition system, based on a farm of power PC processors, the level 4 reconstructs the events completely. On the basis of this information several software filters perform a physiscs oriented selection, i.e. each processor applies a series of selection criteria depending on those subtriggers that the triggered event, for example, one of the most important rejection algorithms relies on the event (x, y, z) vertex constraint. Events that are accepted by the filter farm are permanently stored on tape. L4 also creates separate streams of events for the purpose of monitoring and calibration of some subdectetors. A small fraction of events rejected by L4 are brought off and written to tape to enable monitoring of the effects of the L4 decisions.

Events passing all trigger levels are permanently written to tape in two different formats: physics output tapes (POTs) or in a compressed way on disk named data summary tapes (DSTs). The full events with all raw and reconstructed information are recorded to Production Output Tapes (POT) and stored. On the other hand, DSTs contain only a subset of predominantly reconstructed quantities. The data analized in the present work are stored on DSTs.

Subtrigger S67

As we mentioned before, the subtrigger used in this analysis is $S67$, that is defined by the combination of three conditions from trigger level L1, based on the information provided by LAr. It is defined as:

$$S67 = LAR \quad \&\& \quad T0 \quad \&\& \quad VET \tag{4.1}$$

with && representing the logical condition AND. Thus, the event must satisfy simultaneously the LAR Calorimeter condition (LAR), the timming condition ($T0$) and the veto condition (VET).

24

LAR condition requires the `LAR_electron_1 TE`, i.e., this trigger element is set if the electromagnetic energy deposited in one of the BTs is larger than the amount set as threshold. In CB and FB regions this goes from $\sim 5 GeV$ up to $\sim 25 GeV$ respectively.

*T*0 condition requires `LAR_T0`, i.e., this trigger element fires if at least one of the signal of a TT exceeds the T_0 threshold.

VETO condition uses information of ToF detectors as well as CIP detectors, to accept or reject events according to its timing or topology.

The efficiency with which this trigger identifies electrons was estimated to be larger than 99%, as reported in [42].

Chapter 5

Reconstructing Events

The differential cross-section measurement at a collider such as HERA requires the reconstruction of kinematic variables as close as possible to the parton level. The most relevant kinematic quantities in deep inelastic scattering processes are Q^2 and x.

5.1 Event Kinematics

As we mentioned in chapter 2, the kinematics of a DIS event with a fixed center-of-mass energy may be described by two independent variables for unpolarised beams, as in the case of the HERA I running period. In the case of a transversely polarised electron beam, as in the HERA II running period, it is necessary to complete the process description by determining the azimuthal angle of the scattered electron. In practice, y and Q^2 are experimentally determined and x is obtained by means of the equation (2.5). The H1 detector has nearly 4π coverage of the solid angle in calorimetry. This allows a redundant reconstruction of the scattering kinematics from energy and scattering angles measurments. These different methods are based on the naive quark-parton model thesis, and three of them are briefly described in the following sections.

5.1.1 Double Angle Method

The double angle method is based on the angles θ and γ corresponding to the angle of scattered electron and the inclusive angle of the hadronic final state, respectively. After the identification of the scattered electron, one defines two independent quantities Σ and T as follows,

$$\Sigma = \Sigma_h(E_h - p_{z,h}), \qquad T = \sqrt{\left(\Sigma_h p_{x,h}\right)^2 + \left(\Sigma_h p_{y,h}\right)^2} \tag{5.1}$$

where E_h, $p_{x,h}$, $p_{y,h}$ and $p_{z,h}$ are the components of the four-momentum vector of each hadronic final state particle. Thus, from energy-momentum conservation, the inclusive

angle γ is defined as

$$\tan \frac{\gamma}{2} = \frac{\Sigma}{T}, \tag{5.2}$$

corresponding to the scattering angle of the struck quark in the naive quark-parton model. Then, to reconstruct the event kinematics, we have

$$y_{\theta\gamma} = \frac{\sin\theta(1 - cos\gamma)}{\sin\gamma + \sin\theta - \sin(\theta + \gamma)} \qquad Q_{\theta\gamma}^2 = 4E_e^2 \frac{\sin\gamma(1 + \cos\theta)}{\sin\gamma + \sin\theta - \sin(\theta + \gamma)}, \tag{5.3}$$

and x is given by

$$x_{\theta\gamma} = \frac{Ee}{Ep}\left(\frac{\sin\gamma + \sin\theta + \sin(\theta + \gamma)}{\sin\gamma + \sin\theta - \sin(\theta + \gamma)}\right). \tag{5.4}$$

This method is essential for calibration purposes since the energy response of the detector can be compared to the double angle prediction [39].

5.1.2 Jacquet-Bloded Method

The Jacquet-Bloded method[40] also known as the *Hadron Method*, only takes into account the hadronic final state particles with energies E_i and scattering angles θ_i to reconstruct the inelasticity y.

Replacing the momentum tranfer q in equation (2.2) by $(p_h - p)$, where p_h is the four momentum of the total outgoing hadronic final state and taking into account energy-momentum conservation, after some algebra one obtains,

$$y_h = \Sigma_h \frac{E_h(1 - cos\theta_h)}{2E_e} \qquad Q_h^2 = \frac{p_\perp^2}{1 - y_h} \tag{5.5}$$

where $p_\perp$ is the total transverse momentum of the hadronic flow. The x variable may be derived from equation (2.5) to be $x_h = Q_h^2/sy_h$.

Because the H1 detector does not cover the full 4π angle and since it is not perfectly hermetic, there is leakage of particles and this must be treated carefully. This method is suitable to avoid these effects since the particles which are likely to be lost (mostly in the forward direction) in the beam pipe, have minimal influence because of their small $E_h - p_{zh}$ and $p_\perp$. This method provides a rather good measurement of the inelasticity at low and medium y and degrades at high y. And, its accuracy is determined by these leakage particles.

5.1.3 Electron Method

The kinematics can also be reconstructed with the Electron Method. It is formulated in terms of the scattered electron energy E_e' and polar angle θ_e. Then the reconstruction of

the quantities Q^2 and y can be written[1] as

$$y_e = 1 - \frac{E'_e(1 - \cos\theta_e)}{2E_e} \qquad Q^2 = 2E'_e E_e(1 + \cos\theta_e) = \frac{E'^2_e \sin^2\theta_e}{1 - y_e}. \tag{5.6}$$

The variable x is calculated from equation (2.5) as

$$x_e = \frac{Q^2_e}{sy_e} \tag{5.7}$$

This method gives a very precise Q^2 determination on the whole range and a very precise determination of x at high y with a fast degradation at low y (*i.e.* $y < 0.1$). This method is sensitive to the effects of initial state radiation and is useful for those events with scattered electron well identified at detector level.

For events with the electron scattered into the backward calorimeter($\theta_e > 150$), y depends mostly on E'_e, i.e. if the E_e is low, then y reaches high values. On the other hand, if y has low values (< 0.1), then Q^2 is almost solely defined by the scattered electron angle θ_e.

In H1, both E_e and θ_e are measured using the LAr calorimeter via the energy depositions, mainly recorded in the EM section. This is the method we use to reconstruct our NC kinematics.

5.2   The Breit Frame of Reference

To study the dynamics of the hadronic final state in DIS events, the Breit frame of reference is frequently employed, in order to separate the contribution of hadrons stemming from the dissociation of the proton, from those originating from the struck quark [9, 10].

The z axis of the Breit frame is aligned to coincide with the positive proton axis direction. The transformation from the laboratory reference frame to the Breit frame, experimentally, implies a boost of the DIS events, followed by a rotation, so that the virtual photon momentum points along the negative z axis. The full transformation occurs in the electron scattering plane.

The incoming quark is exactly back-scattered at the boson incoming direction. Because of this, the Breit frame is sometimes called *the brick wall frame*. The particles produced by the interaction may be separated in two regions according to their *z-momentum* p^{BF}_z. The positive region ($p^{BF}_z > 0$) is refered to as the *target hemisphere*, where all proton remnants are spected to be found, this is also known as the spectator system. The negative region is refered to as the *current hemisphere* ($p^{BF}_z < 0$), which is populated by the struck quark. See fig.(5.1).

---

[1]To emphasize that the variables are determined only by the scattered electron the subscript 'e' is added
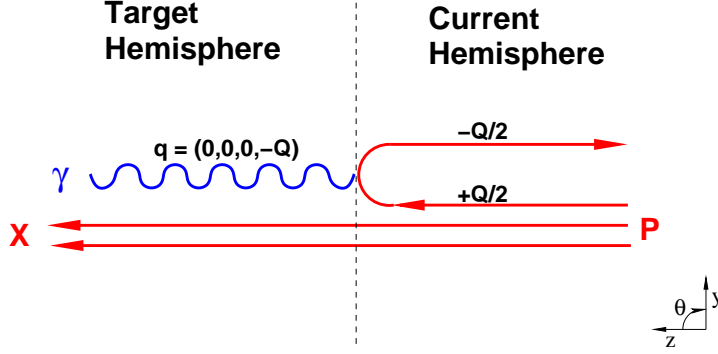
Figure 5.1: Sketch of a simple photon-quark collision in the Breit frame.

In the Breit frame, the exchanged virtual boson is completly space-like. It has zero energy and also zero tranverse momentum, and its z-momentum component is given by $-Q = -2xp^{BF}$, where p^{BF} is the proton momentum in Breit frame, so that the four-momentum transfer is

$$q = (0,0,0, -2xp^{BF}) \equiv (E, p_x, p_y, p_z). \tag{5.8}$$

The advantage of this frame is that it gives a maximal separation of the incoming and outgoing partons in the Quark Parton Model (QPM). Also, the separation in different regions is useful in the case of baryon production, in order to understand the mechanism of baryon-number transfer.

We see that the mechanism of particle production in the current region is analogous to a single hemisphere in $e^+e^- \rightarrow q\bar{q}$ annihilation process, where the quarks produced have equal and opposite momentum $\pm\sqrt{s}/2$. Then, their fragmentation can be compared with the struck quark from the proton which has outgoing momentum $-Q/2$ in our DIS events. The analogy with the annihilation process is improved by the introduction of the fragmentation variable

$$x_p = 2\frac{p^{BF}}{Q}, \tag{5.9}$$

because it corresponds to $x_p = p/p_{beam}$ in the e^-e^+ process. According to QPM the highest momentum a particle may achieve in the current region is $Q/2$, and hence $0 < x_p^{BFC} < 1$, where the superscript BFC refers to the Breit-frame current region. It is expected that the strange quarks produced from the hard interaction ep collisions populate mainly the current region.

30

5.3   Energy Loss dE/dx

The trajectory of a charged particle in CJC is parametrized by a helix, due to the homogeneous magnetic field B_z. However the motion parallel to the beam axis is not affected. Therefore the slope of the helix corresponds to the polar angle of the track. In the transverse plane $(r\phi)$ the curvature is described by a circle. The helix is represented by five parameters: the signed inverse radius of the helix (κ) with the opposite sign to electric charge of the particle, the distance of closest approach with respect to z-axis (DCA), the azimutal angle at DCA (ϕ_{DCA}), i.e. at the starting point of the helix, the polar angle of the track (θ), and the z position at DCA.

The transverse and total momenta p_t and p are derived from the curvature κ by

$$p_t[GeV] = \frac{0.003 \cdot B[T]}{\mid \kappa[cm^{-1}] \mid}, \qquad p = \frac{p_t}{\sin\theta} \qquad E = \sqrt{m^2 + p^2} \tag{5.10}$$

where m is the mass of the particle. The speed of light is set to one, and the Lorentz factors β and γ are defined as

$$\beta = \frac{p}{E} \qquad \gamma = \frac{E}{m} \tag{5.11}$$

The particle crosses the material by an effective lenght L_{eff} given by,

$$L_{eff} = d \cdot \sqrt{1 + \tan^2\phi_{inc} + \cot^2\theta} \tag{5.12}$$

where d is the thickness of the volume, ϕ_{inc} the value of the incidence angle in the transversal plane.

It is well known that relativistic charged particles lose energy, mainly by ionization, when they go through matter, as described by the Bethe-Bloch equation,

$$-\frac{dE}{dx} = Kz^2\frac{Z}{A}\frac{1}{\beta^2}\left(\frac{1}{2}ln\frac{2m_e\gamma^2\beta^2E_{max}}{I^2} - \beta^2 - \frac{\delta(\beta\gamma)}{2}\right) \tag{5.13}$$

where

$\frac{K}{A} = 4\pi N_A r_e^2 m_e c^2/A = 0.307075 \ MeV g^{-1} cm^2$

z the charge of the incident particle in units of e

Z the atomic number of the absorber

I the mean excitation energy of electrons in the absorver

E_{max} the maximum kinetic energy which can be imparted on a free electron in a single collision by an incdent particle of mass m given by

$$E_{max} = \frac{2m_e\beta^2\gamma^2}{1 + 2\gamma m_e/m + (m_e/m)^2} \tag{5.14}$$

31

$\delta(\beta\gamma)$ the density effect correction to ionization energy loss.

The specific energy loss depends on the speed of the incident particle, whilst the tracking detector measures the momentum of the particle. In the following sections there is an attempt to describe how, the specific energy los is determined with our measurements.

5.3.1 Estimation of the Mean Excitation Energy

The measurement of the specific energy loss of charged particles in the H1 central jet chambers (CJC) can be used to identify the particle. Due to the statistical nature of ionisation, fluctuations may ocurr in the amount of energy deposited on the absorber element. The description of these, is characterized by the significance parameter κ, which is proportional to the ratio of mean energy loss ξ to the maximum energy E_{max} allowed to be trasferred in a single collision with an atomic electron

$$\kappa = \frac{\xi}{E_{max}}, \tag{5.15}$$

where

$$\xi = \frac{2\pi z^2 e^4 N_A Z \rho \delta x}{m_e \beta^2 A} = 153.4 \frac{z^2}{\beta^2} \frac{Z}{A} \rho \delta x \qquad keV, \tag{5.16}$$

where ρ is the density of the material, and δx its thickness. Thus κ tends to zero if δx is small and/or if β approaches to 1.

To estimate the average value of the energy loss with the Bethe-Bloch equation it is necesary to limit the model within a certain limit range of material densities and particle energies. Then, $I = 16Z^{09}(eV)$ [38], and the relativistic density effect is not considered.

For a track, given by a set of measurements at the CJC, the predicted specific energy loss defines its most probable value. The statistical fluctuations of a single measurements of the energy straggled of a hit, are computed for the accurancy of the energy loss correction made. In thin layers the energy loss can be described by a Landau distribution. This is an asymmetric distribution, with a long tail at large values. Usually some fraction of hits from the high tail are discardted, known as truncated mean, or also from both tails some fraction may be removed, known as trimmed mean.

In our analysis protons were selected using a procedure based on the likelihood of candidates to be a proton, to achieve a better V^0 vertex fitting.

5.3.2 The Likelihood Method

For the particle identification the treatment of the dE/dx measurement to their tracks is used. As the Landau distribution has an infinite dispersion, the truncated method is used in order to achive a finite dispersion, however this method is less effective due to not use the

full information. In H1 the Likelihood method (LHM) is applied for the dE/dx analysis. This method is briefly described next.

Suppose we want to measure the true value of some quantity Δ_0 in the interval $(\Delta_0, \Delta_0 + d\Delta_0)$, then we have to made N measurements of $\Delta\{\Delta_1, \Delta_2, ..\Delta_n\}$. We assume that the probability distribution function that describes Δ is $\Phi(\Delta, \mu)$. Thus, if the measurements are independent, the probability of getting the measurements we did is

$$L = \prod_i^N \Phi(\Delta_i, \mu) \tag{5.17}$$

this joint probability function is known as *Likelihood* function. For numerical convenience, it is preferable to calculate $\ln L$ than L, thus,

$$\ln L \;\; = \;\; \sum_i^N \ln\Big(\Phi(\Delta_i, \mu)\Big), \tag{5.18}$$

Then, determining the parameter μ, the probability to find Δ at Δ_0 may be known. For a full description of this method see [37].

As mentioned before, for the final particle identification, the dE/dx expectation of the particle is determined under the assumption that the track measured corresponds to a proton. Then, corrections due to saturation and threshold effects [34] are applied. The difference between both values is calculated, and it is used to obtain the likelihood for the particle.

In fig (5.2) the likelihood distribution for the selected protons is shown. Figure (5.3) shows the dE/dx versus the momentum for all tracks in the event triggered. The green (blue) dots represent the events before (after) applying the cut to select only protons with a likelihood larger than 0.003 to be a proton.

The effect of these selections on our mass distributions will be discussed in the last chapter.
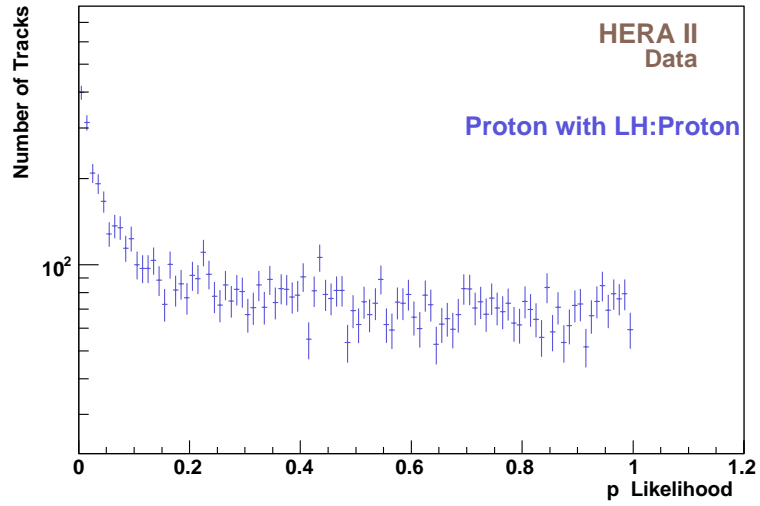
Figure 5.2: Proton likelihood for all tracks in the events triggered.
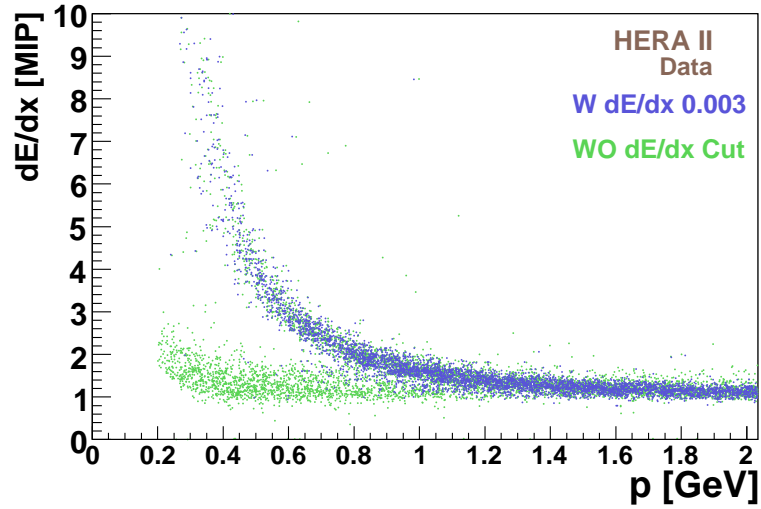
Figure 5.3: dE/dx versus the momentum for all tracks in the event triggered. The green (blue) dots represent the events before (after) applying the cut to select only protons with a likelihood larger than 0.003 to be a proton.

34

Chapter 6

Event Selection and Particle Reconstruction and Identification

¡Milá cuántas montañitas mamá! Matías Bouzas, January 2010.

The HERA facility has provided enough luminosity to carry out many different studies of the proton structure. This has been possible thanks to the presence of multipurpose detectors located along the HERA ring that alow us to select, out of all luminosity events, those within a specific phase-space region of interest. In this work, we study with the H1 detector, the production of the neutral strange Λ baryon state[1] in ep deep inelastic scattering (DIS) at high Q^2 by means of its principal decay mode. In this section we describe the selection criteria that events must satisfy to be accepted four our analysis.

6.1   Selecting Events

Due to enormous quantity of events storage wich cover different physics process, is necesary constrain our data search from the begining, this is possible asking for data filtered online, thus we may do an offline selection.

6.1.1   Run Selection

During data-taking H1 events are collected in so-called *luminosity runs*. A run, refers to a period of at most two hours with experimental conditions kept nearly constant. The runs are taken in a time interval where the HERA luminosity start and the dump or loss of one of the HERA beams form a luminosity fill. Data are recorded in the H1 database

---

[1]Unless otherwise stated, a reference to a state implicitly includes the charge conjugate state.

Period	Run Period	Lumi $[pb^{-1}]$
$2004e^+$	367257-392213	50.61
$2004e^-$	398286-398679	0.15
$2005e^-$	399098-436893	102.93
$2006e^-$	444307-466997	57.73
$2006e^+$	468530-492541	92.54
$2007e^+$	492559-500611	48.02
HERA II	367257 - 500611	351.99

Table 6.1: Integrated luminosities for different data taking periods

every ten seconds, including its integrated luminosity value, as well as other characteristic parameters, as we mention in chapter 4.

In our analysis, for a run to be selected, it must satisfy several requirements,

Subdetector high voltage (HV) status There are some subdetectors which must provide HV-on status, i.e., full functionality during the total run time. In our case, hardware required to have HV status are: CJC 1 and 2, CIP, VETO, LAr, Spac, Lumi, TOF, CaloTrig.

Trigger phase larger than 2 Different trigger phases correspond to different trigger prescale factors if we look into one luminosity fill. This is to avoid the high prescale factors set at the beginning of a luminosity fill, while the tracker high voltage is ramping up, and also to avoid background induced by the beam tuned by HERA machine. This analysis asks for subtrigger 67.

Run luminosity larger than 0.2 nb^{-1} This is to ensure the statistical significance of the analysed data and to avoid short time runs, which were interrupted due to unstable conditions.

Additional quality control There is a list per each period, of some runs well known[2] to be rejected due to different conditions. Some examples of this are: malfunctioning of CIP trigger, LAr Calibration problems, LArHot cells detected, ...

Good or medium run quality The runs are classified as *good*, *medium* or *poor*, depending on the status of the subdetectors and quality of beams at the moment of their taking. This analysis only includes runs labeled as good or medium.

The resulting integrated luminosities, including all mentioned corrections are given in Table (6.1.1). MC events are simulated taking into account the status of the detector

---

[2]Runs quality studies done first by shift crew in turn, and then in offline data quality checks.

for each run separately, thus the same selection of runs applied for data is required for simulated events in order to get the same experimental conditions in both cases.

6.1.2 Event Selection

The data used in this work were collected by the H1 detector during the data-taking period 2004 to 2007. They correspond to a total integrated luminosity of 351.99 pb^{-1} with a center-of-mass energy $\sqrt{s} = 320 GeV$. The analysis starts with $1'941,917$ events.

To reconstruct each event we perform first the identification of the scattered electron. To select an event, its lepton identified as the scattered electron must have a *vertex type one*, which means that it comes from the primary vertex position.

Due to changing beam conditions, the nominal position of the interaction point is not fixed, but it has a gaussian distribution about an average value. This is why we must ensure that the z vertex position (z_{vtx}) of the reconstructed event must lie within the acceptance limits, i.e., we select events with:

$$-35cm < z_{vtx} < 35cm. \tag{6.1}$$

This cut rejects most events which do not come from the nominal interaction region of ep events, as well as satellite bunch interactions.

There are some events with a particle from the hadronic final state (HFS) that fakes the scattered electron. This is the case of the photoproduction processes ($ep \rightarrow eX$, $Q^2 < 0.01 GeV^2$), low Q^2 process ($1 \leq Q^2 \leq 60 GeV^2$), elastic QED Compton process ($ep \rightarrow ep\gamma$), or lepton pair production ($ep \rightarrow eXl^+l^-$). To identify non-ep background events we use the so-called non-ep *background finders*, which are very efficient algorithms dedicated to identify this kind of events. This finders include requirements on the timing of the tracking chambers and the calorimeter signals [43]. In order to improve the rejection of these events, we reject the event if the following two selection criteria are not full filled:

Topological Cut If the event was identified and flagged as background for neutral current (NC) analysis by the background finders, and

$$p_{tbal} < 0.5 \quad \text{or} \quad p_{tbal} > 2.0 \quad \text{and} \quad \eta_{max} < 3 \tag{6.2}$$

where $p_{tbal} = p_{t,HadronsFS}/p_{t,electron}$, and η_{max} denotes the pseudorapidity of the scattered electron.

Timing Cut Ask for the decision of the CJC T0, i.e., if the event does not look like an ep physics event and $\eta_{max} < 3$.

From nearly two-millions events with which we started our selection only $1'271,156$ remain after these cuts are applied.

37

6.1.3 Scattered Electron Selection

Once we restrict our search to the genuine ep interactions, our task is to identify the scattered electron in our events. First of all we must ensure that event has the electromagnetic particle flagged as the scattered electron. Immediatly, it is necesary to verify that our DIS events are only those where the electron was labeled as a candidate in LAr, this is because of the phase-space region of this work.

Next, we take some electron quantities from its reconstructed track such as the energy, θ, etc.

In this analysis, the scattered electron must have an energy

$$E_e > 11 GeV \qquad (6.3)$$

because the efficiency of the LAr to identify it from an energy deposition, taking into account characteristics as shape, size and position, is close to 100%. This cut is used to reduce the background photoproduction events.

The polar angle, which is defined as the angle between z positive axis and the line given by the primary vertex and the center of the cluster of the energy deposited at LAr, as ilustrated in fig (4.4), must be

$$10° < \theta_e < 150°. \qquad (6.4)$$

In this way, we ensure that the event is inside the acceptance of the LAr.

The z_{impact}, defined as impact postition in z of the first electron in the event, must satisfy

$$z_{impact} > -180cm, \qquad (6.5)$$

also to ensure that the electron is inside the LAr acceptance.

In order to achieve the above mentioned LAr efficiency at measurements, there are some fiducial volume cuts applied to remove areas of the EM calorimeter where triggering efficiency is not sufficiently close to 100%. Typically, the inefficiencies are due to trigger cells swiched off due to high noise, or malfunctioning hardware. In fig (6.1) we see the LAr efficiency as a function of the z_{impact} and ϕ cordinates of the impact position, for two different periods of data-taking. There are some trigger cells that were fixed during the course of the experiment. Some regions are neglected only for some periods (blue confined areas), but others must be removed for the entire data taking (red confined areas).

There are two additional selection criteria. We avoid the selection if identification of the scattered electron lies on z or ϕ positions known as $z-crack$ or $\phi-crack$ zones respectively. There are regions, such as the boundary of subdetectors, where the description given by the simulated events do not agree or describe poorly the behaviour of data. Thus, if the identified scattered electron in our event is located at the region between CB1 and CB2, or at the region between CB2 and CB3, then the event is removed from our analysis, i.e if:

$$z_{impact} > -190cm \text{ or } -65cm < z_{impact} < -55cm \text{ or } 15cm < z_{impact} < 25cm \qquad (6.6)$$

38
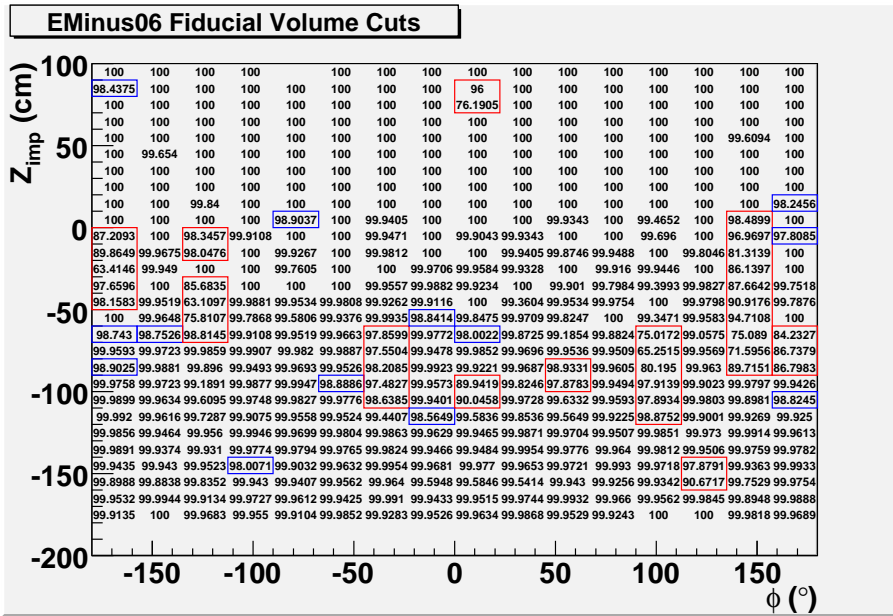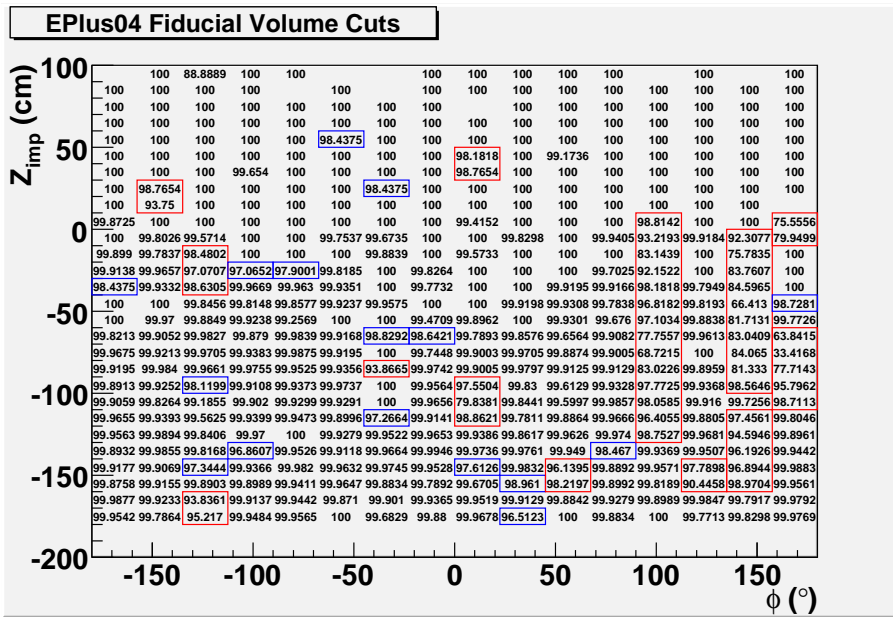
Figure 6.1: The LAr efficiency as function of z_{impact} and ϕ coordinates of the impact position of the first electron. The blue confined area represents regions neglected only for some periods, red confined areas correspond to those removed for the entire data taking.

to avoid z-cracks, and if,

$$\phi_{wheel} \in 2° \text{ around } \phi_{oc} < 2° \text{ or } \phi_{oc} > 43° \tag{6.7}$$

to avoid the ϕ cracks. ϕ_{wheel} corresponds to the ϕ angle determinated on the corresponding wheel of CB (it may be CB1, CB2, or CB3). ϕ_{oc} represents the angle measured within the range covered by each octant of the CB wheels. After this requirements to identify and select our DIS events, we have 862,425 remaining events.

The sum of all energy deposits in the calorimeter allows us to make an energy balance between initial an final states. Theoretically this sum must be equal to twice the electron energy i.e. 55 GeV for DIS if the masses of the electron and proton are neglected. The energy balance condition is given by

$$E - p_z = \sum_i (E^i - p_z^i),$$

where i runs over all calorimeter energy deposits. As this quatity is very sensible to energy losses in the backward direction, it is suited to supress events where the scattered electron is undetected because it escapes through the beam pipe, i.e., initial-state radiation events. Thus we require that our events fullfill,

$$35 < E - p_z < 70 \quad GeV. \tag{6.8}$$

6.1.4   Kinematic Selection

We are interested in baryon yield at high Q^2, specifically Λ production. The visible range defines the phase-space of the analysis, so we select events with negative four-momentum transfer

$$145 < Q^2 < 20,000 \quad GeV^2, \tag{6.9}$$

and inelasticity

$$0.2 < y < 0.6. \tag{6.10}$$

The lower bound for the negative four-momentum transfer implies that we are focused on high Q^2, the upper bound is chosen only to ensure to be within the H1 detector real limits. With respect to inelasticity, is known that if one excludes the events with low y, then to the reconstruction of the kinematics of the event we may do it using the electron method and to obtain the results with a good resolution. This is why we require events to have $y > 0.2$. Furthermore, we introduce an upper limit to the inelasticity $y < 0.6$, in order to reject non-DIS events wich may come from photoproduction or from the interaction of the proton with the beam pipe or the rest-gas whitin it.

After applying the kinematic and technical selection criteria summarized in Table (6.1.4), we have a sample of 377,192 events. With these we may start to reconstruct events yielding Λs.

Selection Criteria	Description
Central vertex	Scattered lepton comes from primary vertex position
$z-vertex$ posistion	$\|z_{vtx}\| < 35$ cm
non-ep Background Cut	Reject if:
	Ep Topological finders fail or $p_{tbal} < 0.5$ or $p_{tbal} >$ 2.0 and $\eta_{max} < 3$
	CJC Timming fail and $\eta_{max} < 3$
Scattered electron	EM particle identified flagged as scattered electron
LAr candidate	electron fired in LAr
Electron Energy	$E_e > 11 GeV$
Electron polar angle	$10° < \theta_e < 150°$
Impact position	$Z_{impact} > -180.0$
Fiducial volume cuts applied	
z-cracks	Reject if $z_{impact} > 15cm$ or $15cm < z_{impact} < 25cm$ or $-65cm < z_{impact} < -55cm$
ϕ-crack	rejected if $\phi \in [2°]$ around $\phi_{oc} < 2°$ or $\phi_{oc} > 43°$
Energy balance	$35 < E - p_z < 70 GeV$
Kinematics	$145 < Q_e^2 < 20000 GeV^2$ and $0.2 < y_e < 0.6$

Table 6.2: Summary of the Event, DIS and kinematic selection criterias used to obtain our final sample.

6.2 Particle Reconstruction

The tracks of the HFS are measured at the central and forward regions. An H1 standard set of track-quality criteria, known as Lee-West selection [44], is applied to all track candidates in order to select *good* tracks and remove the doble-counting due to different hypotheses.

6.2.1 Daugther Tracks Reconstruction

To reconstruct the daugther tracks of our Λ candidates, we are interested only in central tracks measured within

$$20° < \theta < 160°. \tag{6.11}$$

Specifically, we require only central vertex fitted tracks.

In this analysis we search for the strange baryon through its decay $\Lambda \rightarrow p\pi$. Therefore,

we select a Λ if both tracks associated to its daugther particles, proton p and pion π, have opposite charges and meet at the same secondary vertex V^0.

The association of the track to each daugther particle comes from the comparision between the momentum measured for each track. Then, it is set that the track with larger momentum corresponds to the proton, and the other corresponds to the pion.

The distance of closest approach (dca) is the minimal distance between the projection in $x - y$ plane of the track reconstructed associated to a particle, and the origin. Thus, if

$$dca_p \cdot dca_\pi < 0 \tag{6.12}$$

the candidate remain to be tested to next selection criteria.

It is known that the cross-section for multiple interactions with the detector material may increase for decreasing p_t. And also that the tracks with low p_t may curl up within CJC1. Then we set that the tracks must have

$$p_{t,Track} > 0.12 GeV \tag{6.13}$$

The track lenght, which refers to the difference between the coordinates measured at the first and last hits of the track, must be

$$L_{track} > 10 \quad cm. \tag{6.14}$$

L_{track} is measured in $x - y$ plane. With this requirement we attempt to neglect tracks comming from a single charged particle reconstructed as two separate tracks. This may happen specially at the edge between CJC1 and CJC2.

It is important to ensure that the reconstruction of tracks lies within CJC, so we require that the first hit associated to it must be, at least

$$R_{start} < 30 \quad cm, \tag{6.15}$$

from the interaction point.

To ensure that the reconstructed tracks are associated with a V^0 such that their dca's are deemed in an acceptable range, we require that their significance, given by,

$$S_{dca} = \frac{dca}{\delta dca}$$

must be within a limit

$$\mid \frac{dca_\pi}{\delta dca_\pi} \mid < 3 \tag{6.16}$$

for the π track, and

$$\mid \frac{dca_p}{\delta dca_p} \mid < 1 \tag{6.17}$$

for the p track, where δdca refers to the error in the dca measurements.

42
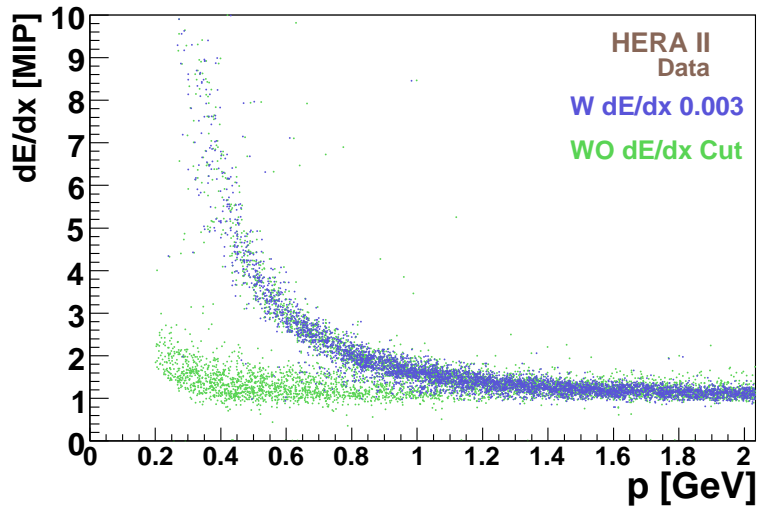
Figure 6.2: *dE/dx vs p* of the proton tracks.

In order to ensure high efficiency for the track reconstruction and particle identification, for each proton track the energy loss dE/dx is determined. The measurement of the particle ionization loss is based on a likelihood method, so we require

$$L_p\Big(\frac{dE}{dx}\Big) > 0.003. \tag{6.18}$$

In fig (6.2) is shown the specfic energy loss versus the momentum of the protons track candidates. In green, measurements for all candidates before (6.18) applying is shown, and in blue, the candidates after this selection criteria.

The applying of the all above selection criterias provide us the opportunity to determine the V^0 in order to reconstruct the neutral strange Λ baryons via its decay daugthers.

6.2.2 V^0 Particle Reconstruction

The Λ invariant mass $M(p\pi)$, is derived from the reconstructed four momentum of the V^0 candidate[3]. The principal decay mode of Λ is

$$\Lambda \to p\pi$$

and represents $63.9 \pm 0.5\%$ of its decay width, see fig (6.3).

For the data selection, two different sets of cuts are introduced, the first to obtain the candidate sample and the second to reduce the background.

---

[3]From here on Λ is refered to the V^0 particle
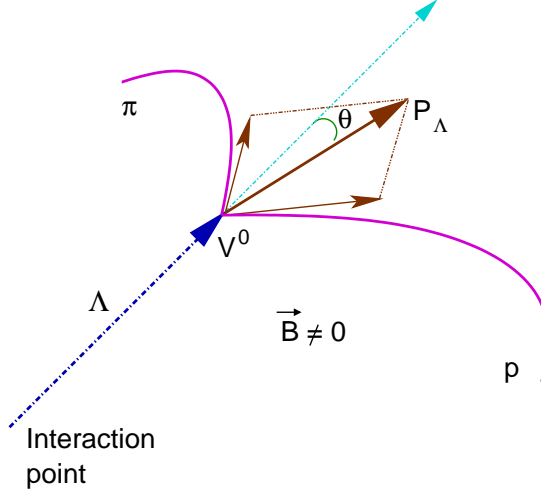
Figure 6.3: Scheme of Λ decay. The Λ produced at the primary vertex travels some distance before it decays. The two detectable tracks associated to daugther particles start at V^0. Due to Λ being neutral its trajectory is undetectable. The angle θ is used in a collinearity cut to remove background.

Thus, once a common vertex is identified for the daughter tracks, only central vertex fitted tracks are chosen to test the selection criteria. The V^0 particle track is constrained to start at primary vertex, so if the fit for a given track converges, the invariant mass of the two tracks is computed as follows:

$$M(1,2) = \sqrt{(E_1 + E_2)^2 - (\vec{p}_1 + \vec{p}_2)^2} \qquad (6.19)$$

where 1 and 2 denotes the daugther particles, and E refers to the energy of the particle track. To compute the energy it is necessary to set a mass hypothesis m for each particle, since

$$E_{daugther} = \sqrt{m_{daugther}^2 + \vec{p}_{daugther}^2}. \qquad (6.20)$$

As with the daugther particles tracks, the p_t of the Λ track is required to satisfy

$$p_t > 0.3 \quad GeV, \qquad (6.21)$$

to achieve a good accurancy to be reconstructed.

The pseudorapidity, defined as $\eta = -ln(tan(\frac{\theta}{2}))$ with θ the polar angle, is required

$$|\eta| < 1.5, \qquad (6.22)$$

in order to ensure a central track, this is due to the geometrical acceptance of the central detectors.

44

The radial decay lenght, measured in $r\phi$ plane, is the distance between the primary and secondary vertices. It is necessary that the V^0 paticle candidate has at least

$$L_{decay} > 2 \quad cm, \tag{6.23}$$

to pass this selection.

The quality of the fit to determine V^0 is constrained to be

$$\chi^2 < 5.4. \tag{6.24}$$

The observable $cos\theta^*$ is computed by performing a boost to the rest frame of the V^0 and then defining θ^* as the angle between the positive track and the direction of the projection of V^0 in that frame. We require that

$$|cos\theta^*| < 0.95 \tag{6.25}$$

to eliminate the posible photoconversion background present ($\gamma \to e^+e^-$), and to ensure high efficiency of track reconstruction and particle identification.

There is a posibility to interpret a K_s^0 as a Λ. This may occur if a pion is missidentified as a proton, in that case we have the reconstruction of the kaon decay channel $K_s^0 \to \pi^+\pi^-$. To remove this kind of contamination to the Λ signal, we take the same tracks as for the Λ to fit again with the hypothesis that the corresponding invariant mass for both daughter particle tracks correspond to pions. If the new fit delivers that the invariant mass of computed for the V^0 particle lies around the nominal value of the K_s^0 mass $M(K_s^0) = 497.614 \pm 0.0024 \ MeV$ [8] then this hypothesis is rejected

$$0.475 \quad GeV \quad < M(\pi^+\pi^-) < \quad 0.53 \quad GeV \tag{6.26}$$

Another criterias to supress the background due to the electron pair production from the photon, is constraining the invariant mass associated to the V^0 track to be larger than 50 MeV in a procedure simmilar to that than employed to avoid the contamination by K_s^0 to the Λ signal.

$$M(e^-e^+) > 50 MeV \tag{6.27}$$

This type of background is generally present when strange particles are reconstructed.

For further analysis, only Λs reconstructed in the mass window

$$1 GeV < M(p\pi) < 1.2 GeV \tag{6.28}$$

about the nominal value of $M(\Lambda) = 1115.683 \pm 0.006 \ MeV$ [8] were retained.

After applying the above-mentioned selection criteria, summarized in Table (6.2.2), the invariant mass distribution of the Λ baryon was obtained.

Selection Criterion	Description
Daugther tracks selection	
Central track	Track within $20° < \theta < 160°$
Two decay daugthers	Number of particles $= 2$
Opposite charge tracks	$dca_p \cdot dca_\pi < 0$
Transverse momentum	$p_{t,Track} > 12 GeV$
Track length	$L_{Track} > 10 cm$
First track hit position	$R_{start} < 30 cm$
Track significance:	$S_{dca,p} < 1$
	$S_{dca,\pi} < 3$
Proton identification	$L\left(\frac{dE}{dx}_p\right) > 0.003$
V^0 Particle identification	
Kinematics	Transverse momentum $p_t > 0.3 GeV$ and
	Pseudo rapidity $|\eta| < 1.5$
Radial decay length	$L_{decay} > 2 cm$
Quality of V^0 determination	$\chi^2 < 5.4$
Avoiding photoconversion	$|cos\theta^*| < 0.95$ and
	$M(e^- e^+) > 50 MeV$
Removing K_s^0 contamination	$0.475 GeV < M(\pi^+ \pi^-) < 0.53 GeV$
Mass window	$1 GeV < M(p\pi) < 1.2 GeV$

Table 6.3: Summary of the track and V^0 particle selection criteria used to obtain Λ invariant mass distribution.

The Armenteros-Podolanski plot

The Armenteros-Podolanski plot illustrate the kinematic properties of the V^0 candidates using two variables, the transverse momentum p_t component of the oppositely charged decay products with respect to the $V0$ particle flight direction,

$$p_T^\pm = p^\pm \sin\theta \tag{6.29}$$

and the longitudinal momentum asymmetry α

$$\alpha = \frac{p_l^+ - p_l^-}{p_l^+ + p_l^-}, \tag{6.30}$$

where p_l is the longitudinal-momentum component of the decay products, also measured from the mother particle flight direction. The positive and negative sign indicate the
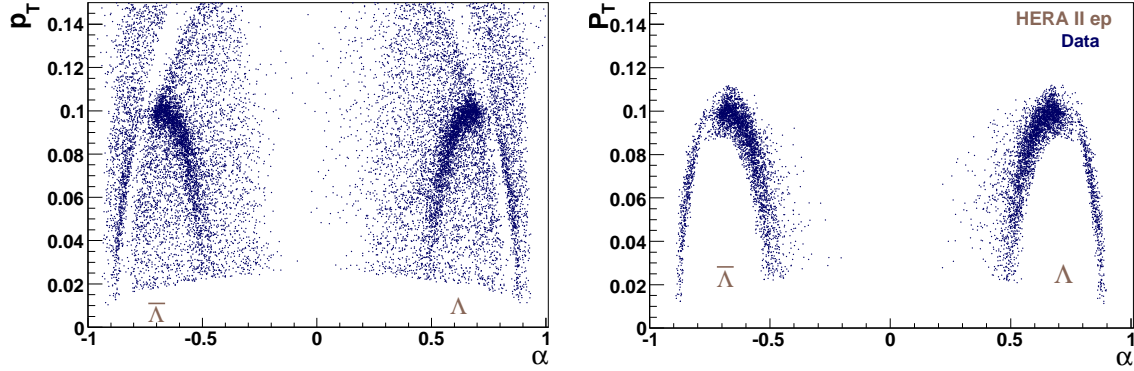
Figure 6.4: Armenteros-Podolanski plot after removed the overlap in masses for V^0 candidates. The $\pi\pi$ mass hypothesis was applied and removed for selected Λ candidates at left. Λ and $\overline{\Lambda}$ selected candidates within a window mass arount the nominal Λ mass at right.

electrical charge of the daughter. The posible decay of V^0 particles form half ellipses. These variables are not used to set a selection criterion for this analysis, but they represent a good tool to do a cross-check to verify our selection.

In fig (6.4) the Armenteros-Podolanski plot, after removing the overlap in masses for V^0 candidates, is displayed. The $\pi\pi$ mass hypothesis, given in equation (6.26), was applied and K_s^0 contamination removed for selected Λ candidates at left panel. The Λ and $\overline{\Lambda}$ selected are presented within a window mass

$$1.10768 GeV < M(p\pi) < 1.12368 GeV \tag{6.31}$$

about the nominal Λ mass at right panel. For the following, the rejection of K_s^0 contamination is applied.

6.3 Λ Identification

The invariant mass spectra of candidates assuming $p\pi$ mass hypothesis for a $V0$ candidate, i.e., for Λ baryons, for all HERA II data is presented in fig (6.5), and reflects 19,648 candidates selected. The fall around $1.07 GeV$ comes from the threshold mass given by p and π masses. We may observe a peak with its high value at $1.1155 GeV$. The purple line correspond to the mass distribution obtained from generated and reconstructed events from Django, and the blue one corresponds to those obtained from Rapgap.

The neutral strange Λ baryon state and its conjugate state $\overline{\Lambda}$, are measured by the kinematic reconstruction of their principal decay mode. As we mentioned before, the track with larger p_T value is assigned to the proton, and antiproton for the antibaryon state. The Λ and $\overline{\Lambda}$ candidates are tagged by the electrical charge of the decay proton and antiproton
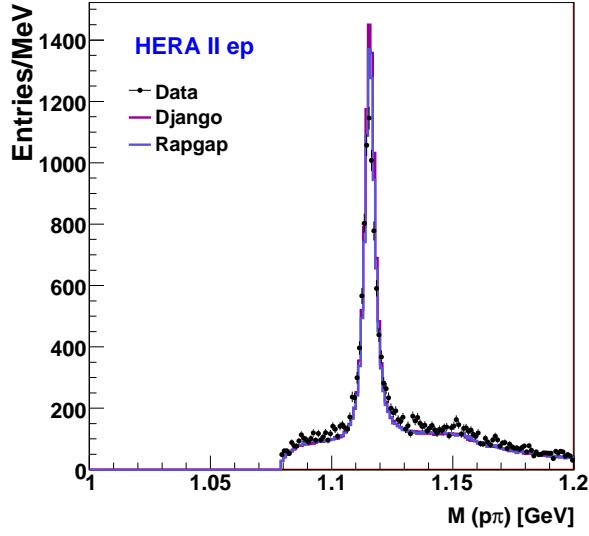
Figure 6.5: Invariant mass spectra of the $\Lambda \to p\pi$ candidates, obtained from our data selected. Black points correspond to observed data points. Solid lines correspond to distributions obtained from generated and reconstructed events by Monte Carlo

respectively. The number of signal particles is obtained fitting simultaneously a signal and a background function to the invariant mass distribution obtained from our selection criteria over all the events.

6.3.1 Signal extraction

The invariant mass spectra was obtained within the mass window $1GeV < M(p\pi) < 1.2GeV$. Due to the threshold mass, the fit to the distribution to determine the number of Λs yielded is done within the range between $(1.08, 1.65)$ GeV.

The function used to fit the peak at the invariant mass spectra is a skewed Student's t distribution,

$$f_{sg}(t) = \frac{\Gamma(\frac{\nu+1}{2})}{\sqrt{\nu\pi}\Gamma(\frac{\nu}{2})}\left(1 + \frac{t^2}{\nu}\right)^{-(\frac{\nu+1}{2})} \tag{6.32}$$

where, ν is the number of degrees of freedom, Γ is the gamma function and t is defined as

$$t = \frac{M - m_\Lambda}{\sigma} \tag{6.33}$$

where M denotes the $p\pi$ invariant mass, m_Λ the nominal value of the Λ, and with the

48
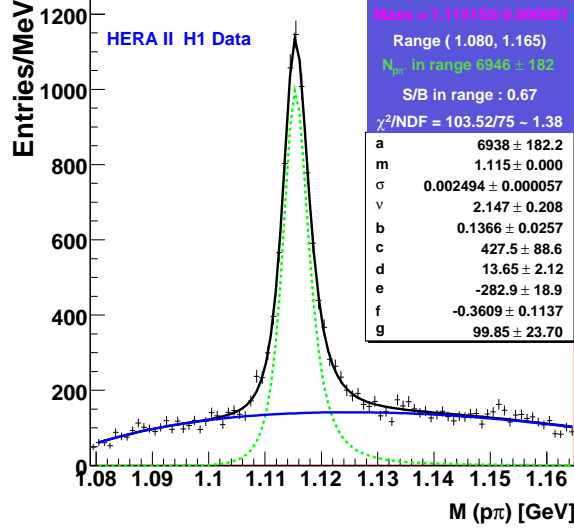
Figure 6.6: Fit to the invariant mass spectrum of the $\Lambda \to p\pi$ candidates obtained from our data selected. Points correspond to the observed data events. Distribution fitted by an skewed Student's t function (green line) and a polynomial background function (blue line).

parameter σ as its standard deviation. The background is described by the function:

$$B_\Lambda(M) = p_0 \ (p_1 + p_2(M - m_\Lambda) + p_3(M - m_\Lambda)^2)(M - (m_p + m_\pi))^{p_4} \qquad (6.34)$$

with m_p and m_π as the nominal masses of the proton and pion, the parameters p_i are extracted from the likelihood fitting procedure.

The fit to the $\Lambda - \overline{\Lambda}$ invariant mass distribution is presented in fig (6.6). The number of $\Lambda + \overline{\Lambda}$ identified for all HERA II period is $N_\Lambda = 6,946 \pm 182$. The mean position of the reconstructed barions is $1.11515 \pm 0.00009 \ GeV$ (statistical only) with a standard deviation of $\sigma = 2.5 \ MeV$, wich is consistent with the value reported by PDG [8]. The resulting fits to mass distributions of Λ and $\overline{\Lambda}$ candidates are shown in figure fig (6.7). As seenHere you may see, there were $N_{p\pi^-} = 3,635 \pm 128$ Λs identified and $N_{p^-\pi^+} = 3,394 \pm 159$ $\overline{\Lambda}$s.

6.3.2 Decay Topologies

There are two different decay topologies observed for a decay process, when the tracks of the daughter particles are inwardly curved or outwardly curved. The fig (6.9) shows a scheme of these decay topologies for $\Lambda \to p\pi$.

The process when the tracks are in-bending is also known as *sailor decay* topology and corresponds to

$$(\overrightarrow{p}_p \times \overrightarrow{p}_\pi)_z < 0. \qquad (6.35)$$
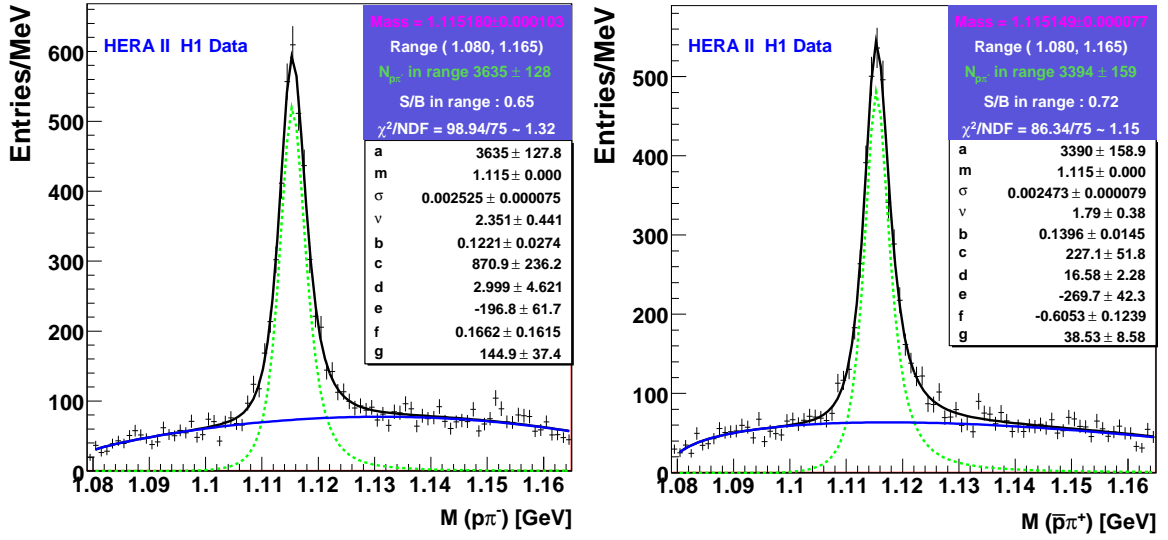
Figure 6.7: Fit to invariant mass distributions of candidates assuming: $M(p\pi^-)$ (left), and $M(p^-\pi^+)$ (right), mass hypothesis for a V^0 candidate. The black solid line represent total fit function, the green dashed line corresponds to signal function and the blue solid line correspons to the background function.
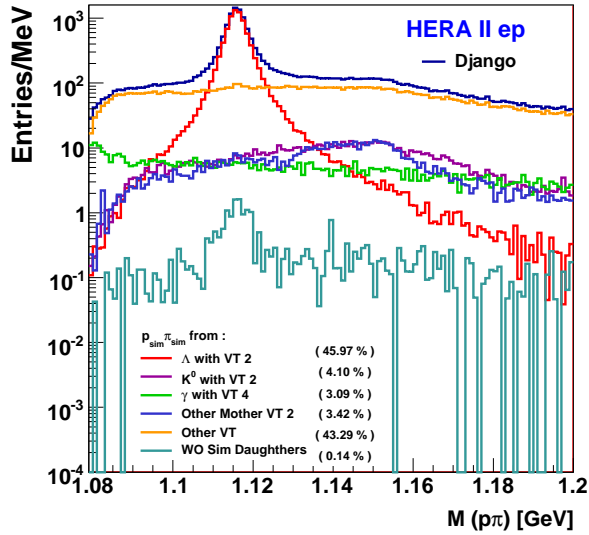
Figure 6.8: Trace back
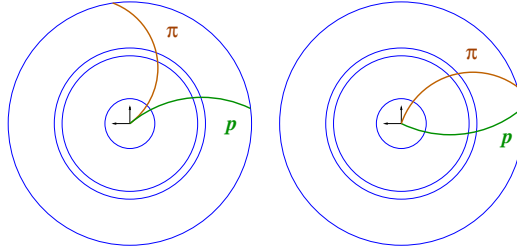
Figure 6.9: Scheme of different decay topologies. When daughter tracks are inwardly curved the process is known as sailor decay topology (right), otherwise, when they are outwardly curved are called seagull decay topology (left)

Otherwise, when tracks are out-bending the product of the z component of their momentum are positive

$$(\overrightarrow{p}_p \times \overrightarrow{p}_\pi)_z > 0, \tag{6.36}$$

and the process is said to be in *seagull decay* topology.

The Λ signal has been studied in these two different decay topologies. In fig (6.10), the fit done to the invariant mass spectra of V^0 candidates is displayed. It can be seen that numbers of Λs identified in each decay topology are very close to each other,

$$N^{Data}_{\Lambda,sailor} = 3524 \qquad N^{Data}_{\Lambda,seagull} = 3482 \tag{6.37}$$

Thus, we may infer both topologies are almost equally sensitive to the track reconstruction resolution.
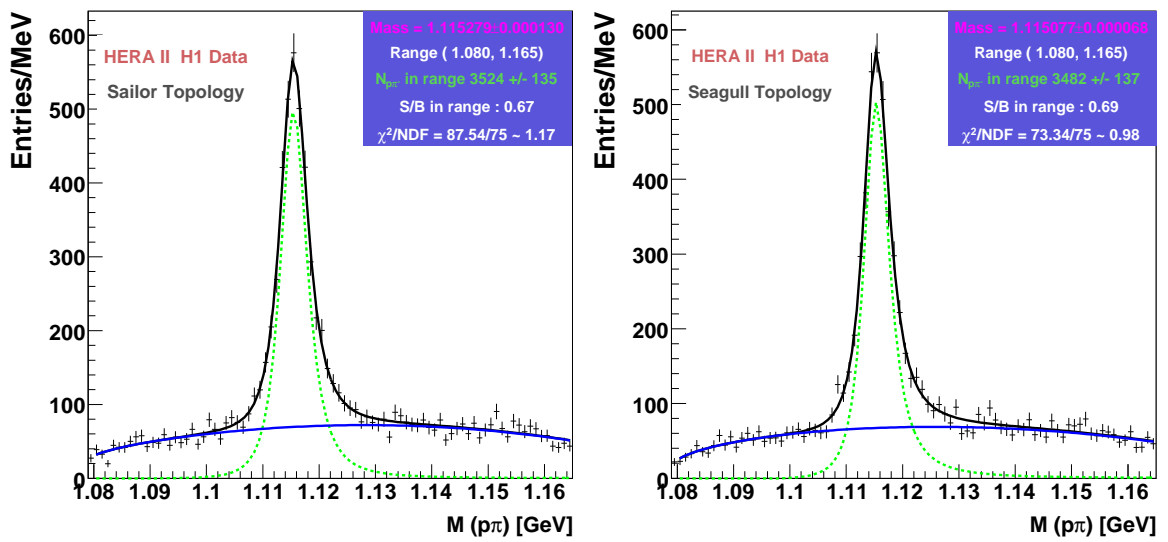
Figure 6.10: Fit to invariant mass distributions of V^0 candidates when the decay process occurs through sailor topology (left) and seagull topology (right).

Chapter 7

Results

In this chapter, the determination of the total cross section of $ep \to e\Lambda X$ in the phase-space

$$145 < Q^2 < 20000 GeV^2 \qquad 0.2 < y < 0.6$$

and

$$p_t > 0.3 GeV \qquad \mid \eta \mid < 1.5$$

is described. First, a brief introduction to method and formulas are given, then the cross section is presented with its contributing systematic errors. At the end of the chapter the asymmetry distributions obtained are presented.

7.1   Cross Section

The cross section in high energy particles area, can be seen as a measure of the probability of interaction between the effective area of a target particle wich may be hit by a point-like projectile when both interacts. In general, the cross section of a particle production during a given interaction can be seen as:

$$\sigma = \frac{N}{\mathcal{L}}$$

where N represents the number of particles of interest yielded by the interaction, and $\mathcal{L}$ is the luminosity. In order to obtain a measure of the cross section independent from the experiment, and to be easly compared with results from other experiments, the data are corrected for the detector acceptance and QED radiation effects. Thus, the total inclusive cross section in the accesible kinematic region σ_{vis} for $ep \to e\Lambda X$ is given by:

$$\sigma_{vis}(ep \to e\Lambda X) = \frac{N_\Lambda}{\mathcal{L} \cdot BR \cdot \epsilon} \cdot (1 + \delta_{dE/dx}) \tag{7.1}$$

where $\mathcal{L}$ denotes the integrated luminosity, BR the branching ratio of the reconstructed decay chanel ($\Lambda \to p\pi$), ϵ is the total experimental correction factor and $\delta_{dE/dx}$ the correction due to $L(dE/dx)_p$ of proton track selection. In this work the value of the integrated luminosity is $351 \ pb^{-1}$.

The total experimental correction factor is given by,

$$\epsilon = \epsilon_{det} \cdot (1 + \delta_{QED}) \cdot \epsilon_{trigger} \tag{7.2}$$

where ϵ_{det} correction for detector effects, δ_{QED} the correction to Born level, i.e. corrects the hadron level for effects from QED radiation, and $\epsilon_{trigger}$ is the trigger efficiency.

7.1.1 Experimental Correction Factor

As we mention in chapter 3, the simulated events independent from the detector effects are said to be on the hadron level $N^{Had}_{MC,NoRad}$. The simulated events passed through the detector simulation and reconstruction algorithms are said to be on the detector level $N^{Det}_{MC,Rad}$.

A cross section corrected for detector effects are known as hadron level cross section. There is an intermediate level between detector level and hadron, it is known as radiative hadron level.

In the radiative hadron level the simulated events take into account photons radiated $N^{Had}_{MC,Rad}$, if the angle between the scattered electron and the radiated photon is smaller than $\alpha_{e\gamma}$ [1], then the photon is removed from the HFS, if not, then it is treated as part of HFS.

The case in which the photon is radiated within an angle smaller than $\alpha_{e\gamma}$ can not be resolved on the detector level, however at hadron level, it may be distinguished. For those events ϵ_{det} and $(1 + \delta_{QED})$ have a large values. However, this effect is cancelled with the separation into contributions from the detector and from higher order QED effects.

As seen figure (7.1), from the reconstructed mass distribution obtained with CDM with $\lambda_s = 0.286$ at left and the obtained with MEPS with same λ_s value at right, we have

$$N^{Det}_{Dja,Rad}(\Lambda) = 7936 \pm 151 \qquad (N^{Det}_{Rap,Rad}(\Lambda) = 7337 \pm 147) \tag{7.3}$$

As the value of trigger efficiency is $\sim 100\%$, the total experimental correction factor is

$$\epsilon^{CDM} = 0.2194 \qquad (\epsilon^{MEPS} = 0.2268) \tag{7.4}$$

The values above obtained are the input for the estimation of the uncertainty of the inclusive cross section, due to model dependence, as will be presented in the following sections.
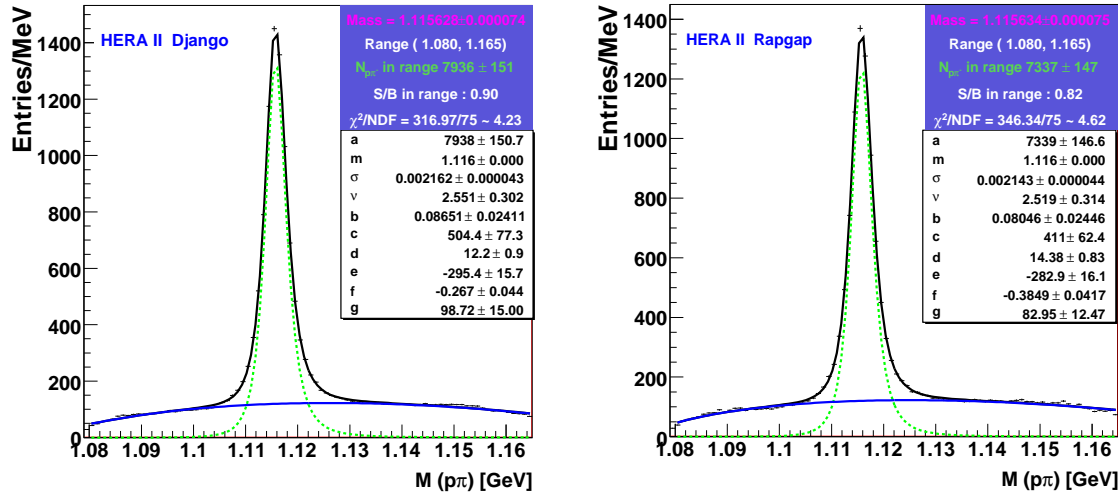
Figure 7.1: Reconstructed Λ mass spectra obtained with CDM(MEPS) with $\lambda_s = 0.286$ at left(right).
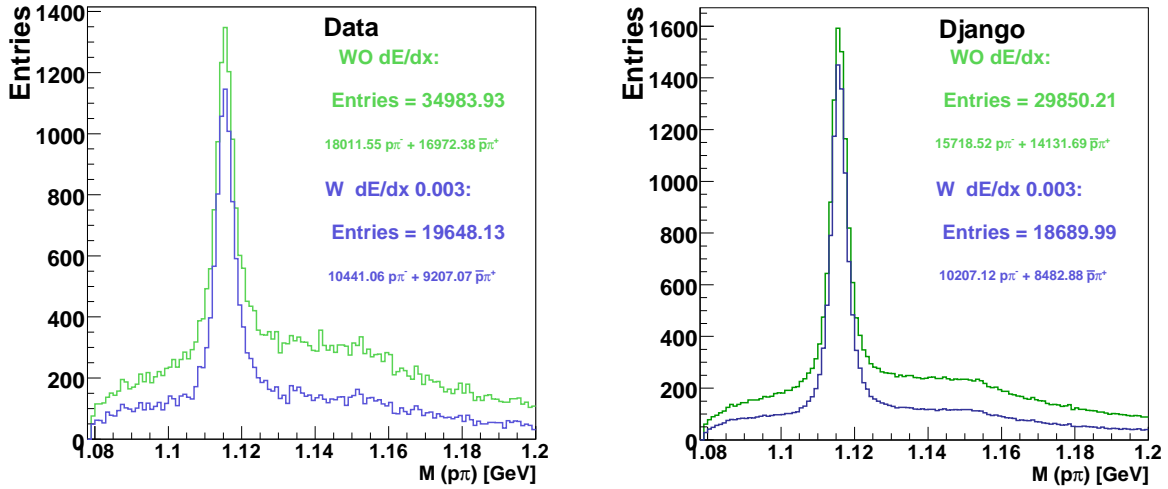
Figure 7.2: Invariant mass spectra of V^0 candidates reconstructed from: protons which their tracks full fill the condition of $L(dE/dx)_p > 0.003$ to be a proton, in blue; and candidates reconstructed without any likelihood hypothesis, in green. At left data distribution, at right CDM distribution.

7.1.2 dE/dx Correction Factor

The measure of the specific energy loss of charged particles in CJC is used to identify protons in our analysis. As seen in Chapter 6, an important reduction on the number of proton candidates is obtained. The variation $\Delta E_{p\pi}^{Data}$ due to this selection, to the invariant mass spectra is shown in fig (7.2) where the blue line corresponds to V^0 candidates reconstructed from protons which satisfy the selection criteria given by equation (6.18). The green line represents the candidates obtained without any likelihood hypothesis to the protons tracks is required. From the figure

$$\Delta E_{p\pi}^{Data} = \frac{E^{WdE/dx}}{E^{WOdE/dx}} = 0.56$$

There is a variation also observed on the simulated events due to this requirement. The variation $\Delta E_{p\pi}^{CDM} = 0.63$. Then, as $\Delta E_{p\pi}^{Data} \neq \Delta E_{p\pi}^{CDM}$ it is necesary to estimate the correction to the inclusive cross section yielded by this difference.

To avoid the correlation between the sample of events which fullfill the $L(dE/dx)_p > 0.003$ condition, and those events obtained without any likelihood hypothesis, we focus on the sample of events rejected, i.e. events reconstructed from proton tracks accepted when $L(dE/dx)_p < 0.003$ condition is required. In fig (7.3), the fits to the reconstructed mass spectra obtained for these two samples are shown. The top figure corresponds to data and the bottom one to MC.

Thus, if $N_{p\pi}^{LhL}$ is the number of Λs identified of events selected with protons with $L(dE/dx)_p < 0.003$ to be a proton, and if $N_{p\pi}^{WOLh}$ is the number of Λs identified of events without any likelihood hypothesis, then, taking

$$R_{Dat} \quad = \quad \frac{N_{p\pi}^{LhL}}{N_{p\pi}^{WOLh}} \quad = \quad 0.06529, \tag{7.5}$$

and computing same ratio for MC events, there is a difference observed between data and MC. From this difference, the correction factor due to the likelihood hypothesis applied to select the protons is estimated as

$$\begin{aligned} \delta_{L(dE/dx)} \quad &= \quad R_{Dat} - R_{MC} \\ &\hookrightarrow \quad 2.8\% \end{aligned} \tag{7.6}$$

This correction must be applied to the inclusive cross section as indicated in equation (7.1).

7.1.3 Systematic Uncertanties

The determination of cross section is subject to systematic uncertainties. The H1 Collaboration had to have several working groups dedicated to estimating and improving the

---

[1]The value of $\alpha_{e\gamma}$ should be close to the resolution of LAr calorimeter. Studies agree to set $\alpha_{e\gamma} = 5°$
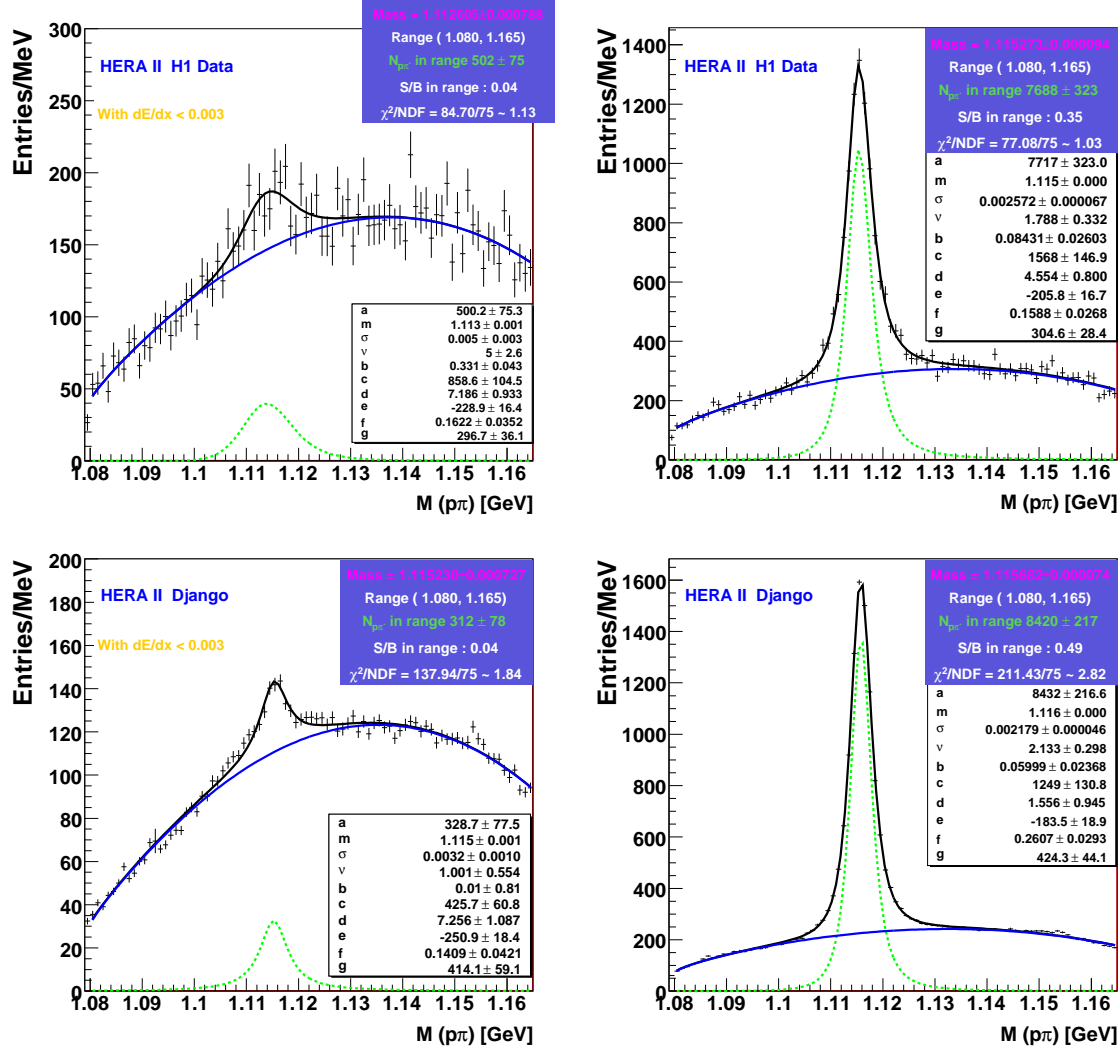
Figure 7.3: Fit to reconstructed Λ mass spectra for events when $L(dE/dx)_p < 0.003$ to proton tracks is required (top-left), and, to the mass distribution of events from protons without any likelihood hypothesis applyed (top-right). At bottom, the fits to the corresponding MC samples are shown.

57

precision of measurement of some observables in order to keep the size of these uncertainties to a minimum value. The sources of systematics errors considered in this analysis are

- Variation $\pm 0.5\%$ of energy of scattered electron,
- Variation $\pm 1 mrad$ of θ_e,
- Variation due to model dependence $\frac{1}{2} \frac{\epsilon^{CDM} - \epsilon^{MEPS}}{\epsilon^{CDM}}$,
- Variation due to signal extraction,
- Variation due to in and out bending topology,
- Variation due to dE/dx,
- Variation in luminosity measurement,
- Track reconstruction,
- Branching ratio,
- Variation due to trigger efficiency.

The procedures to estimate each contribution to the total systematic error are described next.

Electron energy and polar angle

The energies of the clusters candidates are taken on the electromagnetic scale of LAr after the applied corrections of dead material. Additional calibration factors are applied to determine the energy of the scattered electron E_e. These yield that, the electromagnetic energy scale is known within $\pm 0.5\%$ of accuracy for electrons with $z_{impact} < 100cm$ and $\pm 1\%$ for $z_{impact} > 100cm$. On the other hand, the polar angle measurement of the electromagnetic clusters is known within $\pm 1\ mrad$ of precision.

To determine the influence of these uncertainties to cross section measurement, we require, for generated events, a shift up(down) in 0.5% to the value of E_e and $1\ mrad$ up(down) to the value of θ_e, separately. The fits to the invariant mass spectras reconstructed with CDM when shifts above mentioned are applied are shown in fig (7.4). The Λs identified from these distributions, $N_{p\pi}^{EeUp}$, $N_{p\pi}^{EeDw}$, $N_{p\pi}^{TeUp}$ and $N_{p\pi}^{TeDw}$ respectively, are used to compute the cross section for each case. Thus, the variation to the inclusive cross section due to these shifts may be quantified as

$$\triangle\sigma_{source}(\Lambda) = \frac{\sigma - \sigma_{source}}{\sigma} * 100 \tag{7.7}$$

where σ is the inclusive cross section.

The efficiency, total cross section and systematic error yielded by shifts on E_e and θ_e are presented in Table (7.1).

58
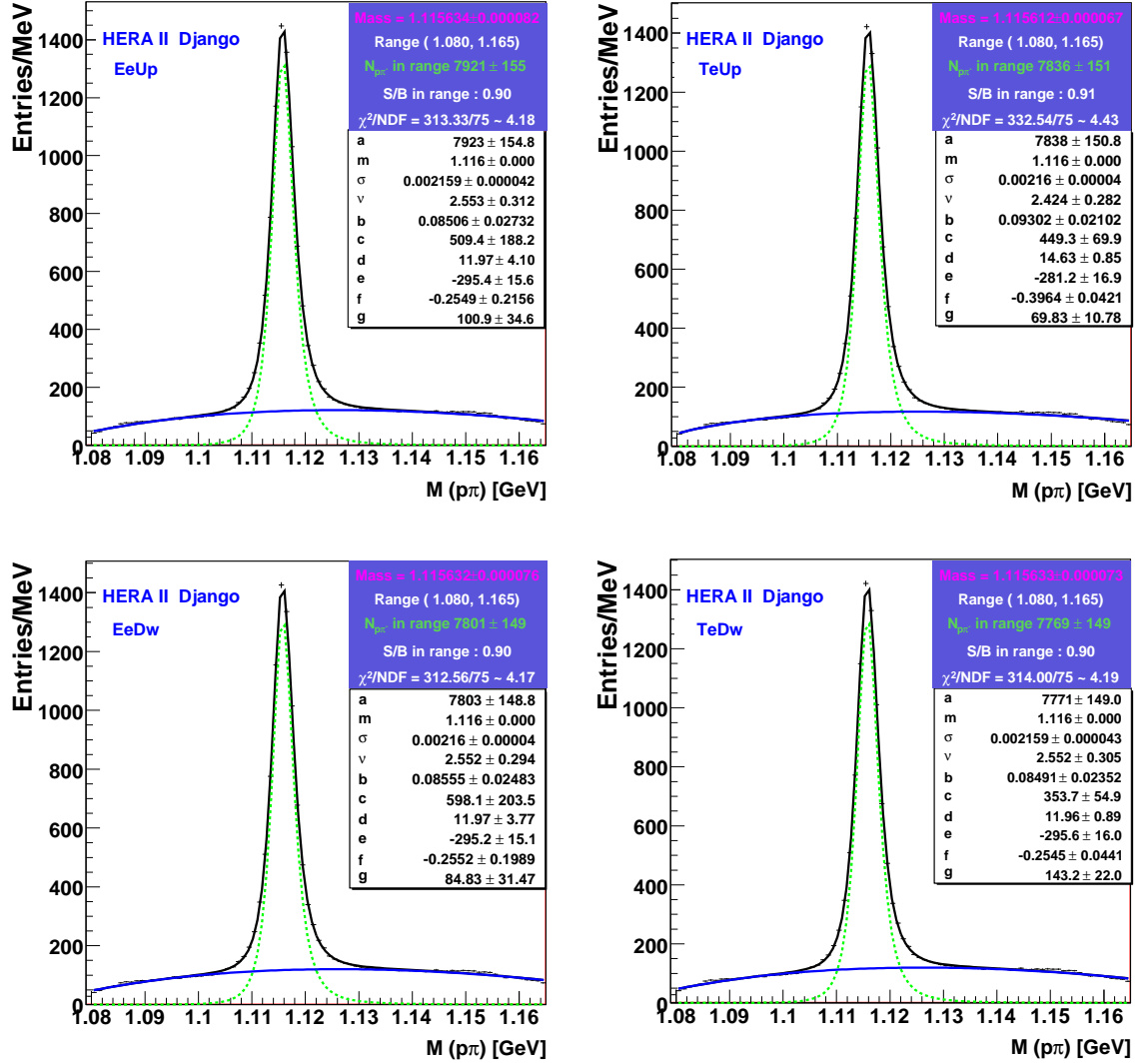
Figure 7.4: Fit to Λ mass distribution reconstructed with Django when E_e is shifted up(down) at top(bottom) at left and, θ_e is shifted up(down) at top(bottom) at right.

Source	ϵ^{CDM}	σ_{source} [pb]	$|\triangle\sigma_{source}(\Lambda)|$ [%]
$E_e + 0.5\%$ $(EeUp)$	0.2190	141.025	2.54
$E_e - 0.5\%$ $(EeDw)$	0.2156	143.187	1.05
$\theta_e + 1$ mrad $(TeUp)$	0.2167	142.548	1.48
$\theta_e - 1$ mrad $(TeDw)$	0.2148	143.779	0.63

Table 7.1: Contribution to total systematic uncertainty yielded by shifts on E_e and θ_e.

Model dependence

In general our data are well described by the MC simulations used in this analysis, but there are regions where this description is only reasonably good. This is why it is necessary to obtain the detector correction factor from MC. If we compare two different MCs to estimate the correction factor, they are going to be different. This differences must to be taken into account.

As seen in equation (7.4), the correction factor for the inclusive cross section obtained when CDM with $\lambda_s = 0.286$ is used to estimate the correction, differs from that obtained when MEPS with the same value of the strangeness supresion factor is used. Then,

$$\begin{aligned} \triangle\sigma_{ModDep}(\Lambda) &= \frac{1}{2}\frac{\epsilon^{CDM} - \epsilon^{MEPS}}{\epsilon^{CDM}} \cdot 100 \\ &\hookrightarrow 1.68\% \end{aligned} \tag{7.8}$$

This is the uncertainty derived from the model dependence used to correct our cross section measurement.

Signal extraction

The uncertainty derived from the signal extraction, i.e. the error to determine $N_{p\pi}$, must be computed. This is done by comparing the number of Λs identified from the fit to the invariant mass distribution (N_Λ^{Fit}), and the number resulting by simple counting after substracting the expected background (N_Λ^{SBS}) within the sub-range $(1.102, 1.14)$ GeV. Then,

$$\Delta\sigma_{sigex}(\Lambda) = \left| \frac{N_\Lambda^{Fit} - N_\Lambda^{SBS}}{N_\Lambda^{Fit}} \right| \tag{7.9}$$

where

$$N_\Lambda^{SBS} = N_\Lambda^{Count} - N_\Lambda^{NewBgFit}, \tag{7.10}$$

with N_Λ^{count} the number of Λ counted within the mass window, and $N_\Lambda^{NewBgFit}$ the background contribution to the signal peak estimated within this sub-range.
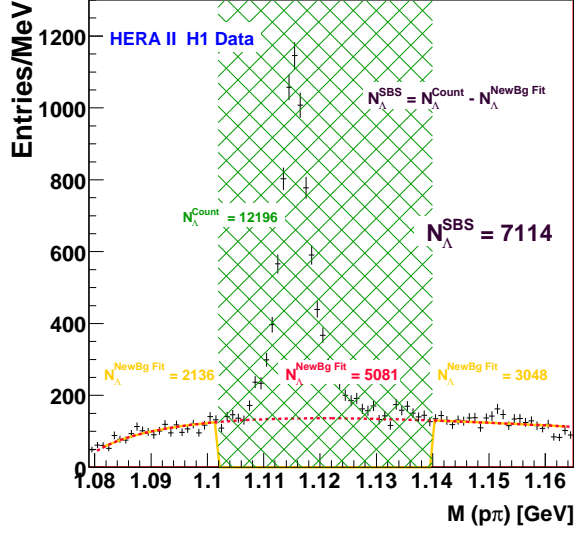
Figure 7.5: The invariant mass spectra with the fit to the background with the new fit function as the solid orange line, and the extrapolation of this within the sub-range as the dashed red line. Numbers showed correspond to number of Λs estimated at their corresponding zone

To estimate the background contribution, a different background function is defined, given by,

$$B_\Lambda(M) = p_0 \, exp^{p_1 + p_2(M - m_\Lambda)} (M - (m_p + m_\pi))^{p_3} \tag{7.11}$$

which describes the behaviour of background in a good manner. Then, this function is used to fit the side bands out of the mass window and to extrapolate to the inner range to estimate $N_\Lambda^{NewBgFit}$.

The invariant mass spectra with the mass window delimited by the dashed green area is seen in fig (7.5). The solid orange line corresponds to the fit to the side bands with the new background fit function. The dashed red line represents the extrapolation of the function within the sub-range. The numbers showed correspond to the number of Λs estimated at their corresponding zone.

Thus, the uncertainty estimated due to signal extraction is,

$$\Delta\sigma_{sigex}(\Lambda) = 2.4\%. \tag{7.12}$$

In the case of the differential cross sections measurements, the sub-range where the N_Λ^{SBS} is estimated, is defined within each bin of each kinematical variable.

Topology

As seen in equation (6.37), Λ has two different decay topologies, and there is a small difference between them, with almost 2% more Λs yielded from the inbending (sailor) topology than those yielded by outbending (seagull) topology. To estimate the uncertainty due to Λ decay topologies it is necessary to compute the cross section for each decay topology, and then compare them with the inclusive cross section. Then,

$$
\begin{aligned}
\triangle\sigma_{topology}(\Lambda) &= \frac{\sigma_{Tot} - (\sigma_{sailor} + \sigma_{seagull})}{\sigma_{Tot}} * 100 \\
&\hookrightarrow 0.17\%
\end{aligned}
\tag{7.13}
$$

This is the contribution from different decay topologies to total systematic uncertainty.

Energy loss

The selection of the proton tracks under the likelihood assumption $L_p(dE/dx) > 0.003$ to be protons yields a better accuracy on the proton selection than the case when protons are selected without any likelihood requirement. In section 7.1.2, the analysis to determine the correction factor to be applied to the inclusive cross section was done with the sample of events rejected when this criteria was applied, and when there was not any hypothesis about the likelihood of the proton track.

The estimation of the uncertainty contribution from this source to the total systematic error is determined in a similar manner. From the sample of events originally rejected, i.e. Λs reconstructed from protons with tracks with $L_p(dE/dx) < 0.003$ we obtain $N_{p\pi}^{LhL}$, and from the sample without any likelihood requirement we obtain $N_{p\pi}^{WOLh}$. If

$$
\Delta R = \sqrt{\left(\frac{\Delta N_{p\pi}^{LhL}}{N_{p\pi}^{WOLh}}\right)^2 + \left(\frac{N_{p\pi}^{LhL}\Delta N_{p\pi}^{WOLh}}{(N_{p\pi}^{WOLh})^2}\right)^2}
$$

Then, for data and MC we get, $\Delta R_{Dat} = 0.010$ and $\Delta R_{MC} = 0.0093$ respectively. Thus,

$$
\begin{aligned}
\Delta\sigma_{L(dE/dx)}(\Lambda) &= \sqrt{(\Delta R_{Dat})^2 + (\Delta R_{MC})^2} \\
&\hookrightarrow 1.4\%
\end{aligned}
\tag{7.14}
$$

This is the amount of the contribution to the total uncertainty.

Luminosity

The error in the luminosity measurement leads to a normalization uncertainty. The integrated luminosity of the HERA II period has been determined with a precision of 2.3% as reported in [45] . Thus,

$$
\Delta\sigma_{Lumi}(\Lambda) = \pm2.3\%
\tag{7.15}
$$

corresponds to the systematic uncertainty due to the luminosity measurement.

Track reconstruction

The uncertainty due to charged particle track reonstruction was estimated as 2% per track, as was reported in H1 after studies to tracks that curl up at CJC, where they are reconstructed after passing through some dead material. Therefore,

$$\triangle\sigma_{TrackRec}(\Lambda) = \pm4\% \tag{7.16}$$

represents the systematic uncertainty due to the Λs daughter tracks reconstruction. This turns out to be the dominant source of systematic error in our analysis.

Branching ratio

Variation due to branching ratio

$$\triangle\sigma_{BR}(\Lambda) = \pm0.5\%. \tag{7.17}$$

Trigger efficiency

The efficiency achieved with the trigger used in this analysis to identify the electron was estimated to be larger than 99 %, as quoted in section 4.2.4. Thus,

$$\triangle\sigma_{Trigger}(\Lambda) = \pm1.0\% \tag{7.18}$$

represents the statistical uncertainty of the trigger efficiency.

7.1.4 Summary of the Systematic Uncertainties

The summary of the contributions of all systematic uncertainties is shown in Table (7.2). Due to the nature of the source of the errors, they may be considered as *correlated* or *uncorrelated*. That is, if the error depends of any of the variables under investigation, then it is considered as correlated. On the contrary, the common uncertainties, are labeled as uncorrelated, for example the value of the luminosity uncertainty which is reported by the H1 Collaboration.

Generally the correlated errors are studied bin by bin in the case of the differential cross section. For the present analysis, only the values of the uncertainties from the electron energy and polar angle, the model dependence and the signal extraction, are computed in each kinematical bin. The total systematic error is obtained as the sum of systematic contributions added in quadrature.

63

Source	Variation	$\Delta\sigma_{source}(\Lambda)$ [%]
E_e	$\pm 0.5\%$	$+2.54/-1.05$
Θ_e	$\pm 1 mrad$	$+1.48/-0.63$
Model Dependence	$\frac{1}{2}\frac{\varepsilon_{rec}^{CDM}-\varepsilon_{rec}^{MEPS}}{\varepsilon_{rec}^{CDM}}$	± 1.68
Signal Extraction	$\frac{N_\Lambda^{Fit}-N_\Lambda^{SBS}}{N_\Lambda^{Fit}}$	± 2.4
Topology		± 0.17
$L\left(\frac{dE}{dx}\right)_p > 0.003$		± 1.4
Luminosity		± 2.3
Track Reconstruction		± 4.0
Branching Ratio		± 0.5
Trigger		± 1.0
Total systematic error		$+6.47/-5.89$

Table 7.2: Contribution of systematics uncertainties considered at the present analysis. The contribution of the first five sources are computed for $p\pi^-$ and $\overline{p}\pi^+$ independently.

7.1.5   Inclusive Cross Section Measurements

The inclusive Λ cross section σ_{vis} is measured in the phase-space given by $145 < Q^2 < 20000$ GeV^2 and $0.2 < y < 0.6$, for the ranges $p_t > 0.3 GeV$ and $|\eta| < 1.5$. The production of the sum of Λ and $\overline{\Lambda}$ baryons is found to be

$$\sigma_{vis}(ep \rightarrow e[\Lambda + \overline{\Lambda}]X) = 144.70 \pm 4.68(\text{stat})\binom{+9.36}{-8.52}(\text{sys})pb \qquad (7.19)$$

where the first error is statistical and the second is the systematic. As shown, the error of the measurement is dominated by the systematic uncertainty.

The individual Λ and $\overline{\Lambda}$ production rates are measured to be

$$\sigma_{vis}(ep \rightarrow e\Lambda X) \;\; = \;\; 72.60 \pm 3.25(\text{stat})\binom{+4.75}{-4.45}(\text{sys})pb \qquad (7.20)$$

$$\sigma_{vis}(ep \rightarrow e\overline{\Lambda}X) \;\; = \;\; 72.89 \pm 4.01(\text{stat})\binom{+4.88}{-4.56}(\text{sys})pb \qquad (7.21)$$

These are found to be consistent with each other within the statistical accurancy.

[pb]	CDM ($\lambda_s = 0.22$)	CDM ($\lambda_s = 0.286$)	MEPS ($\lambda_s = 0.22$)	MEPS ($\lambda_s = 0.286$)
$\sigma_{vis}(ep \to e[\Lambda + \overline{\Lambda}]X)$	136	161	120	144
$\sigma_{vis}(ep \to e\Lambda X)$	68	81	61	73
$\sigma_{vis}(ep \to e\overline{\Lambda}X)$	68	80	59	71

Table 7.3: Cross sections predictions from MonteCarlo simulations for the production of the sum of Λ and $\overline{\Lambda}$ baryons, and individual production rates.

The cross sections obtained from Monte Carlo simulations are shown in Table (7.3), for CDM and MEPS with two different values for λ_s, 0.286 and 0.22. Comparing the values measured with those predicted by models, it may be concluded that, for:

$\sigma_{vis}(ep \to e[\Lambda + \overline{\Lambda}]X)$ the measured value is in agreement with the expectation of CDM when $\lambda_s = 0.22$ and with the expectation of MEPS when $\lambda_s = 0.286$.

$\sigma_{vis}(ep \to e\Lambda X)$ the measured value is in agreement with the expectation of CDM when any of the two λ_s values are used, and with MEPS when $\lambda_s = 0.286$.

$\sigma_{vis}(ep \to e\overline{\Lambda}X)$ the measured value is in agreement with the expectation of CDM when any of the two values of λ_s are used, and with MEPS when $\lambda_s = 0.286$, as in case of its charge the conjugate state.

7.2 Differential Cross Section

The measurements of the differential cross sections are obtained in the same visible range as for the inclusive cross section. They are performed in bins of x, Q^2, p_T and η, for the laboratory frame of reference, and in bins of x_p^{BF} and p_T^{BF} variables, for both current and target regions, for the Breit frame of reference. The differential cross section of the investigated variable ξ, is given by,

$$\frac{d\sigma_{vis}(ep \to e\Lambda X)}{d\xi} = \frac{N_\Lambda(\Delta\xi)}{\mathcal{L} \cdot BR \cdot \epsilon(\Delta\xi) \cdot \Delta\xi}, \tag{7.22}$$

where $\Delta\xi$ is the bin width of the variable ξ, $N_\Lambda(\Delta\xi)$ is the number of Λs in this bin and $\epsilon(\Delta\xi)$ is the efficiency computed for this bin. The binning size used for the kinematic reconstruction was chosen based on the resolution of the H1 detector and the statistics of the sample. The efficiencies are determined bin by bin.

7.2.1 Binning Scheme

The measurement of the differential cross section of a variable is divided into discrete bins. The size of these bins results very important to avoid or minimize migration effects, and at the same time, to have as many as possible measurements of the differential cross section to obtain more information about Λs.

$Q^2[GeV^2]$	x	η	$p_T[GeV]$	x_p^{BFC}	x_p^{BFT}	$p_T^{BF}[GeV]$
145 , 167	0.0024 , 0.004	-1.5 , -0.5	0.3 , 0.8	0.00 , 0.07	0.00 , 0.07	0.00 , 0.35
167 , 200	0.004 , 0.008	-0.5 , 0.0	0.8 , 1.1	0.07 , 0.13	0.07 , 0.13	0.35 , 0.60
200 , 280	0.008 , 0.017	0.0 , 0.45	1.1 , 1.55	0.13 , 0.20	0.13 , 0.20	0.60 , 1.00
280 , 500	0.017 , 0.200	0.45 , 0.95	1.55 , 2.23	0.20 , 0.33	0.20 , 0.33	1.00 , 1.80
500 , 1000		0.95 , 1.5	2.23 , 3.5	0.33 , 1.0	0.33 , 1.0	1.80 , 14.00
1000 , 5000			3.5 , 14.0		1.0 , 2.0	

Table 7.4: Binning scheme defined for the present analysis.

The binning scheme defined for the present analysis for each variable investigated is shown in Table (7.4).

7.2.2 Purity and Stability

The term *migration* refers to the fact that there are events whose can be reconstructed in the wrong bin because of the finite resolution of the detector, or QED effects, etc. Migration may occur from the bin under investigation to a higher or lower one, or viceversa. This effect is verified by means of the Monte Carlo simulation. There are two variables that help with this task, the *purity* and *stability*, defined as

$$P = \frac{N_{rec,gen}(i)}{N_{rec}(i)} \tag{7.23}$$

and

$$S = \frac{N_{rec,gen}(i)}{N_{gen}(i)} \tag{7.24}$$

where $N_{rec}(N_{gen})$ denotes the total number of MC events that are reconstructed (generated) in a bin (i) but possibly generated (reconstructed) in another bin $(j \neq i)$, and $N_{rec,gen}$ denotes to the number of events that are both generated and reconstructed in the same bin (i).

For a better understandity, we may define the counterpart of each of those two quantities. The purity allows us to evaluate the resolution of our binning scheme, in order to

66

avoid the *impurity* which reflects the migration into the bin. This depends on the distribution and resolution in neighbourings bins. On other hand, the stability enable us to avoid the *inestability* which tells us about the migration out of the bin. This depends only on resolution and distribution within the bin.

The purity and stability distributions corresponding to $[\Lambda + \overline{\Lambda}]$ production are presented in fig (7.6). The distributions corresponding to Λ production are shown in figure (7.7) and those corresponding to $\overline{\Lambda}$ are shown in figure (7.8) .

Both, the purity and the stability typically exceed 80% for all bins of all variables in laboratory frame, and are larger than 90% for kinematical variables in the Breit frame. This confirms that the migration effects for the chosen binnig scheme are small.

7.2.3   Correction Factors

In analogy with what was presented in section 7.1.1, the differential cross section at hadron level is obtained when detector effects are corrected in the measured values. As done for the inclusive cross section, we use CDM with $\lambda_s = 0.286$ to do the correction. Values of the correction factor estimated with MEPS with the same value for the strangeness correction factor are used to compute model dependence uncertainty described in next section.

The correction factor is given by

$$\epsilon_i^{MC} = \left(\frac{N_{MC,Rad}^{Det}(i)}{N_{MC,NoRad}^{Had}(i)} \right), \tag{7.25}$$

where $N_{MC,Rad}^{Det}(i)$ denotes the number of events reconstructed at detector level within bin i, and $N_{MC,NoRad}^{Had}(i)$ denotes the number of events generated at hadron level within the bin i.

The corresponding distributions for $[\Lambda + \overline{\Lambda}]$ production are shown in figures (7.9) for laboratory and Breit frame variables respectively.

The distribution of the correction factor obtained as function of the four-momentum squared Q^2 of the photon and the transverse momentum p_T of the Λ take values between (0.15-0.30). When it is obtained as function of the pseudo rapidity η and the variable x, the correction factor take values within (0.20-0.25). In the Breit frame, it is observed that the correction factor estimated as function of x_p^{BF} at the target region and p_T^{BF} in any hemisphere, varies from 0.19 to 0.27, while as a function of x_p^{BF} in the current hemisphere, the distribution of the correction factor is spread within (0.13-0.25).

The correction factor distributions obtained in Λ and $\overline{\Lambda}$ productions independently are shown in figures (7.10) and (7.11) respectively. The behaviour of the distributions as functions of each variable obtained for Λ and $\overline{\Lambda}$ productions independently of each other, are the same as described above for the total $\Lambda + \overline{\Lambda}$ production.
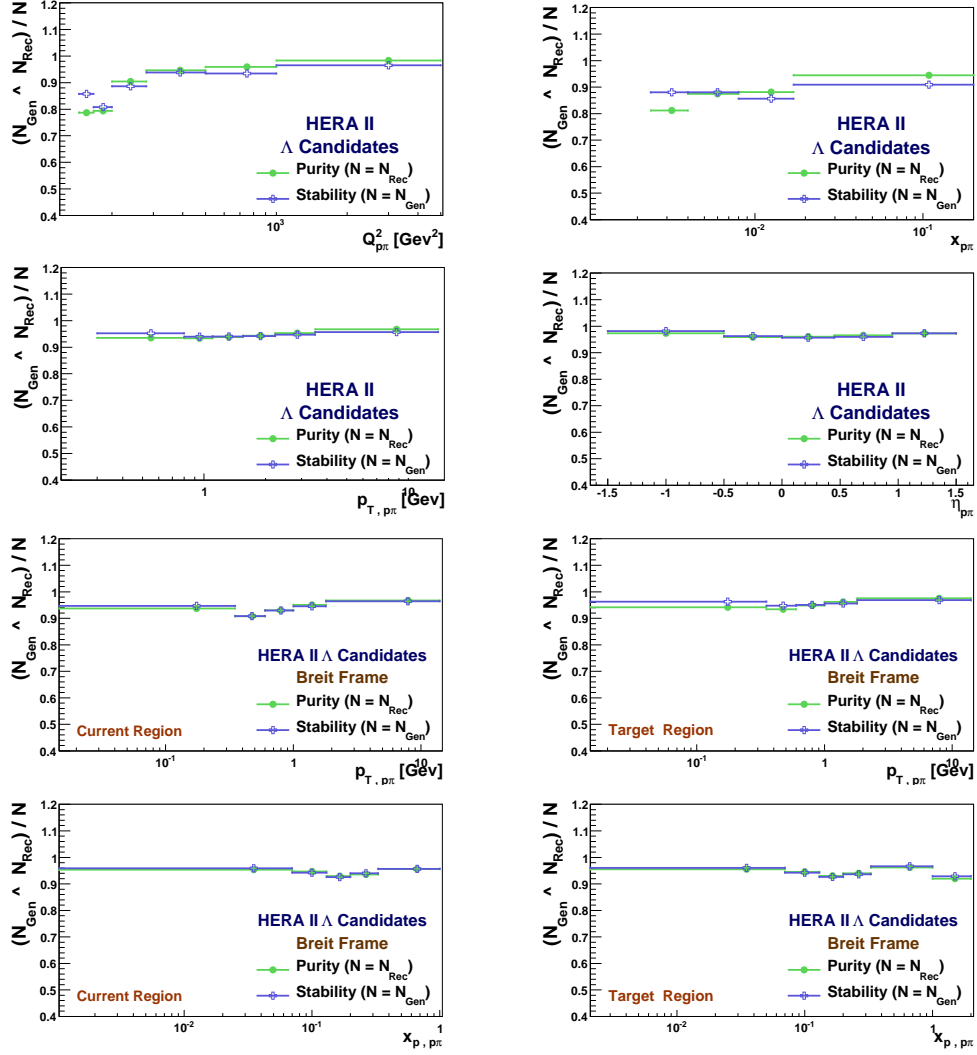
Figure 7.6: The purity(green line) and stability(blue line) for $[\Lambda + \overline{\Lambda}]$ baryons as a function of the kinematic variables Q^2, x, p_t and η, and as a function of the kinematic variables p_t^{BF} and x_p^{BF} in target and current hemispheres of the Breit frame. Distributions obtained with CDM.
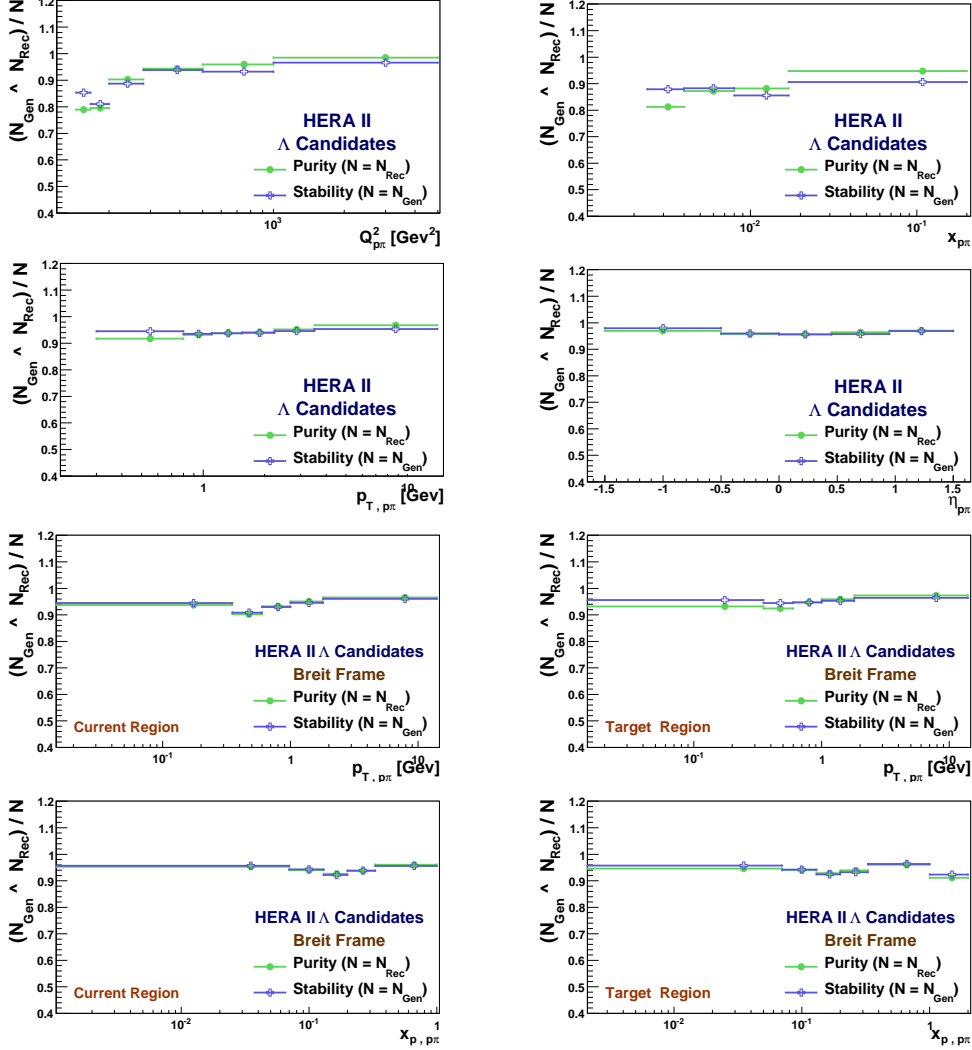
Figure 7.7: The purity(green line) and stability(blue line) for Λ baryons as a function of the kinematic variables Q^2, x, p_t and η in laboratory frame, and as a function of the kinematic variables p_t^{BF} and x_p^{BF} in target and current hemispheres of the Breit frame. Distributions obtained with CDM.
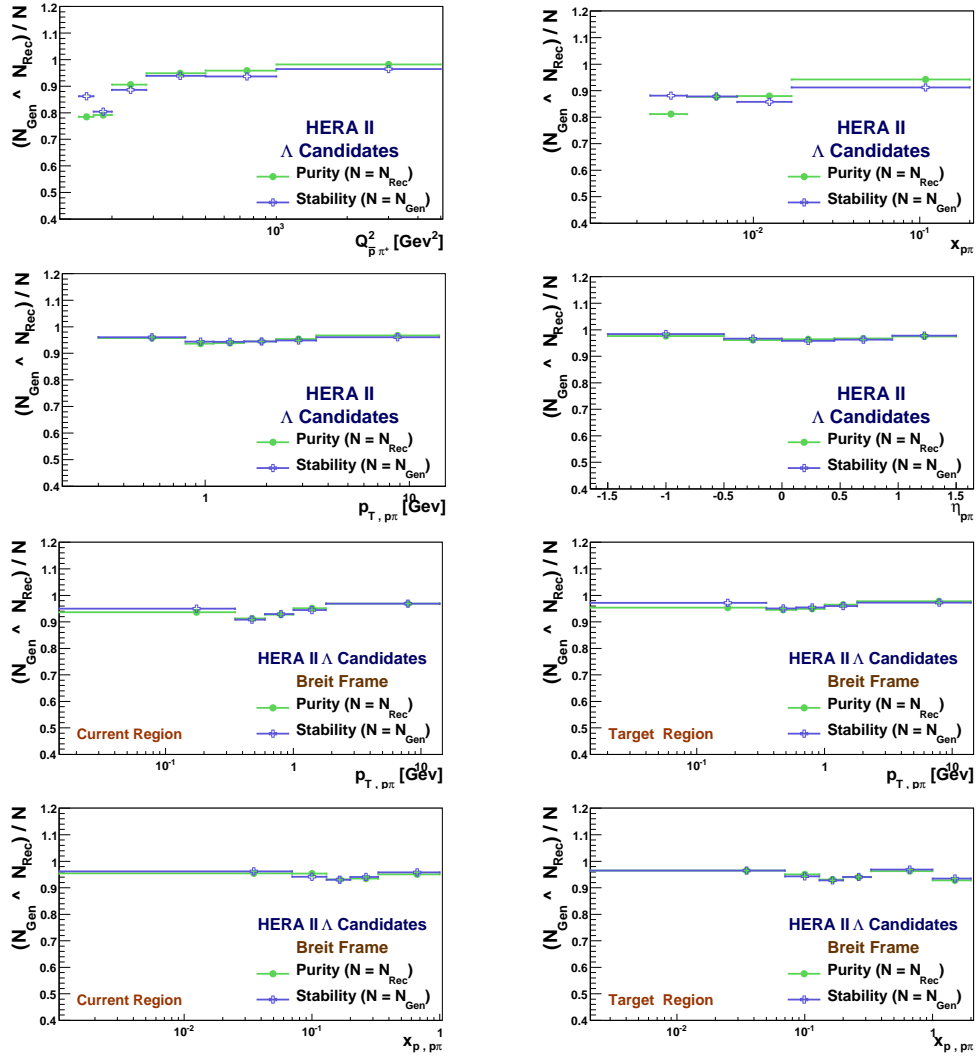
Figure 7.8: The purity(green line) and stability(blue line) for $\overline{\Lambda}$ baryons as a function of the kinematic variables Q^2, x, p_t and η in laboratory frame, and as a function of the kinematic variables p_t^{BF} and x_p^{BF} in target and current hemispheres of the Breit frame. Distributions btained with CDM

70
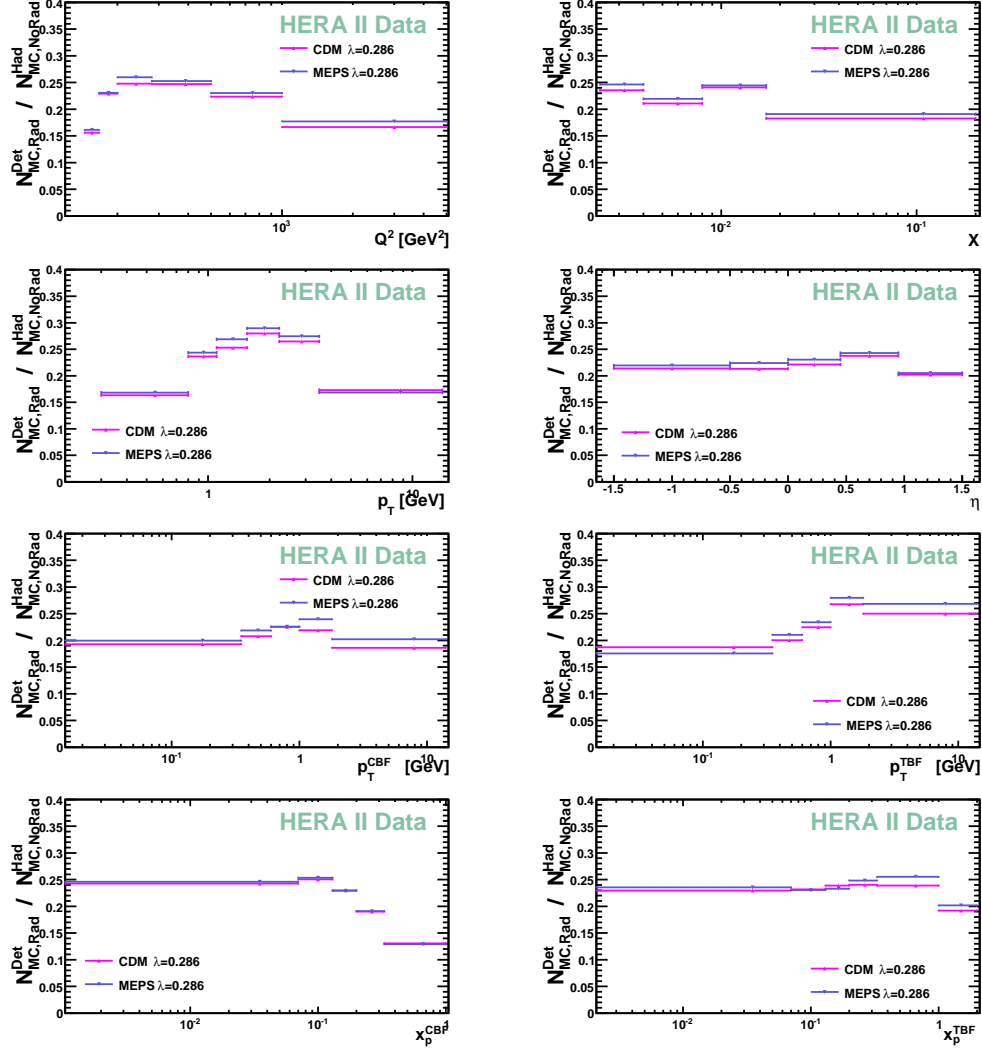
Figure 7.9: The CDM(magenta line) and MEPS(blue line) correction factors obtained for $[\Lambda + \overline{\Lambda}]$ baryons as a function of the kinematic variables Q^2, x, p_t and η in laboratory frame, and as a function of the kinematic variables p_t^{BF} and x_p^{BF} in target and current hemispheres of the Breit frame

71
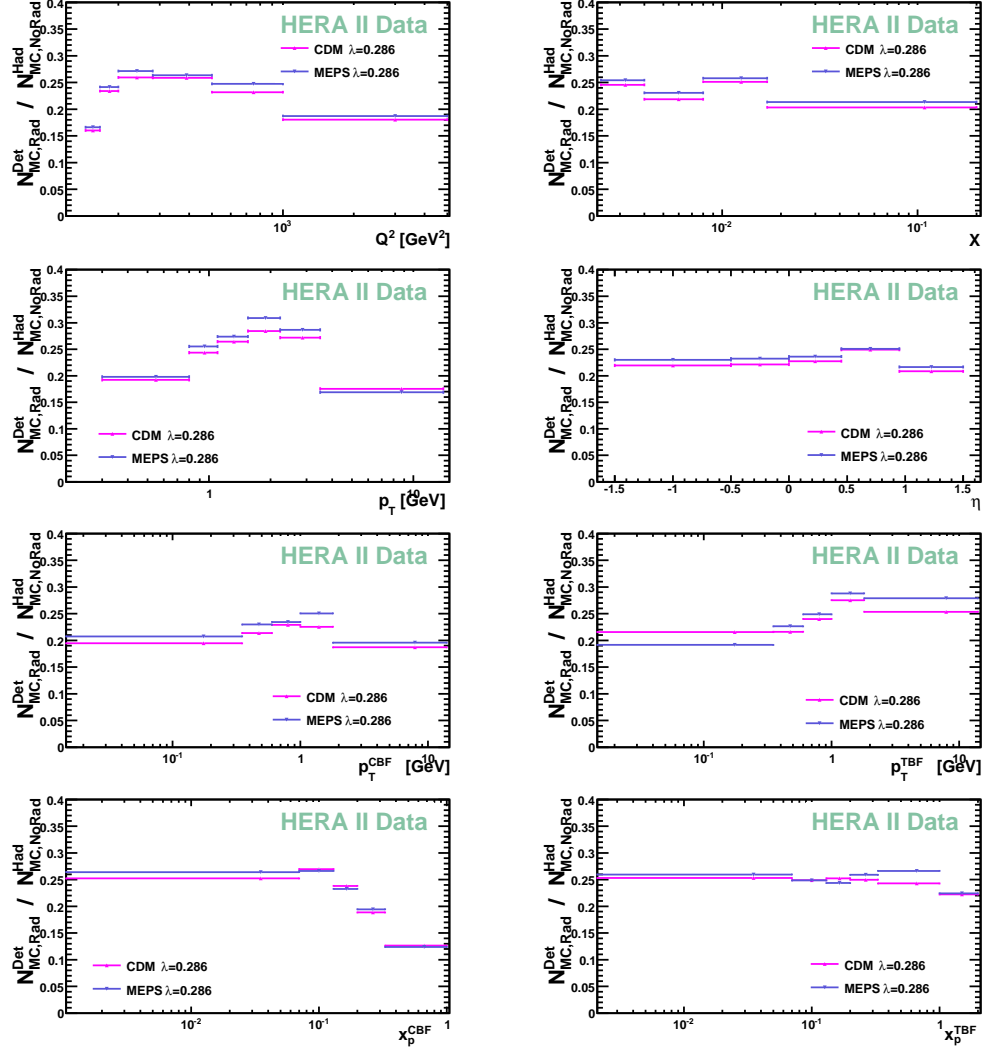
Figure 7.10: The CDM(magenta line) and MEPS(blue line) correction factors obtained for Λ baryons as a function of the kinematic variables Q^2, x, p_t and η in laboratory frame, and as a function of the kinematic variables p_t^{BF} and x_p^{BF} in target and current hemispheres of the Breit frame

72
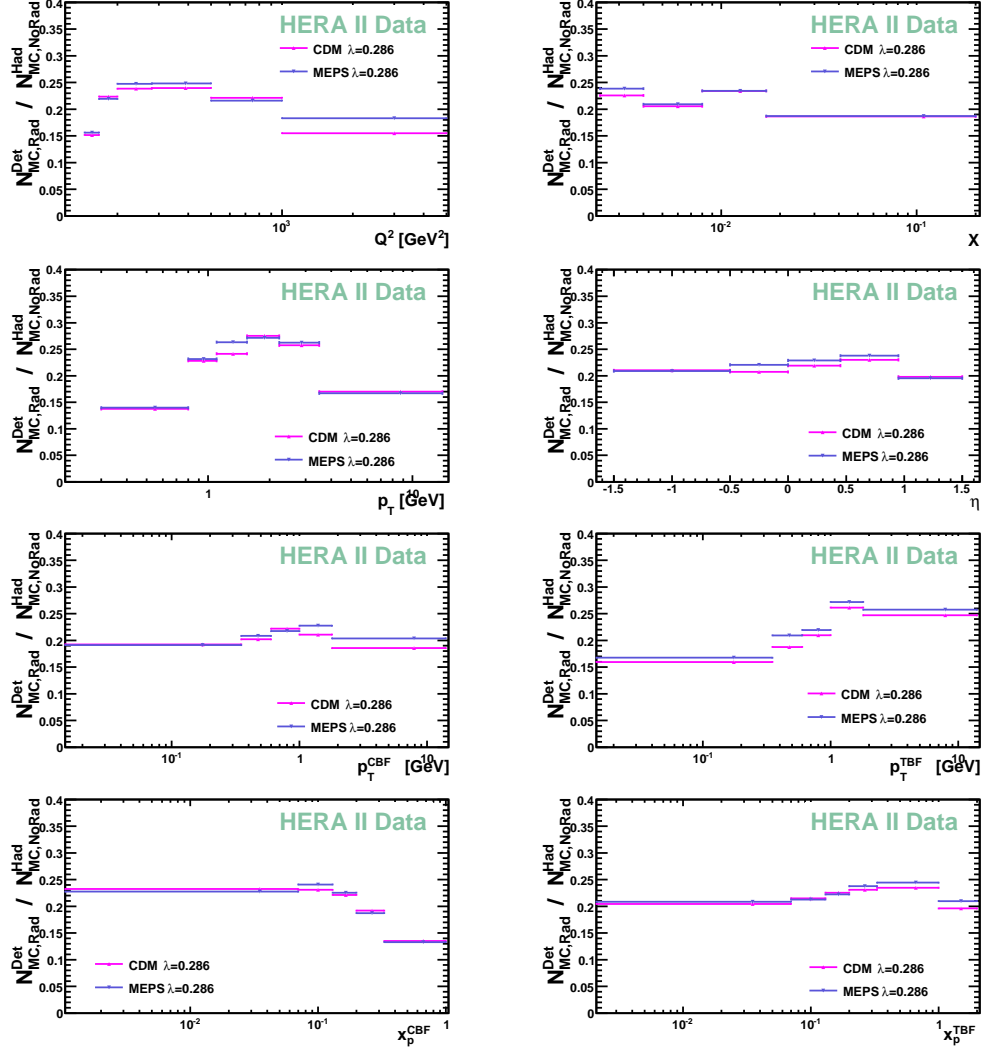
Figure 7.11: The CDM(magenta line) and MEPS(blue line) correction factors obtained for $\overline{\Lambda}$ baryons as a function of the kinematic variables Q^2, x, p_t and η in laboratory frame, and as a function of the kinematic variables p_t^{BF} and x_p^{BF} in target and current hemispheres of the Breit frame.

7.2.4 Systematic Uncertainties

As mentioned in section 7.1.4, there are two systematic error categories, correlated and uncorrelated ones. It is expected that all the correlated errors are estimated for each bin of all events and kinematical variables. However, there are cases where this is not possible, for example, when the statistic in a bin is too low.

Then from the list of sources of systematic uncertainties considered for the inclusive cross section, and summarized in Table (7.2), only the contribution of the first four sources are computed for each bin, and the other two correlated uncertainties, the one given by the different decay topology and the other given by applying likelihood criteria to proton's track selection, are set for all bins as follows,

Different decay topology For $[\Lambda + \overline{\Lambda}]$ production this uncertainty is set to $\Delta\sigma_{topology}[\Lambda + \overline{\Lambda}] = 0.17\%$. In the case of baryon production $\Delta\sigma_{topology}(\Lambda) = 0.05\%$ and for antibaryon $\Delta\sigma_{topology}(\overline{\Lambda}) = 3.25\%$, as was computed for the entire sample.

$L(dE/dx)_p > 0.003$ For $[\Lambda + \overline{\Lambda}]$ production, and when Λ and $\overline{\Lambda}$ are independently studied, the contribution of this source is set to be 3.1%, where it is taken into account the correction factor from section 7.1.2, and the systematic error reported previously.

Thus, the contribution due to shifts on the measure of electromagnetic energy and to the polar angle of the scattered electron, and variations coming from the dependence on the model used to correct the differential cross section, and those derived from the signal extraction are computed bin by bin. The contribution of the uncorrelated uncertainties are set as in the case of the inclusive cross section.

7.2.5 Differential Cross-Section Measurements

The differential cross sections for $[\Lambda + \overline{\Lambda}]$ production in laboratory frame as a function of the photon virtuality squared Q^2, the Bjorken variable x, the transverse momentum p_T and the pseudorapidity η are presented in figure (7.12). All figures show in the upper part the cross sections measured and corrected with CDM model with $\lambda_s = 0.286$, and the predictions from CDM and MEPS for both values of strangeness supression factor $\lambda_s = 0.286$ and $\lambda_s = 0.22$ are displayed. The error bars shown represent the total (outer bars) and statistical (inner bars) errors. At the bottom of each plot, the ratio $MC/Data$ are appended for the prediction of the different MC models.

The cross sections decrease rapidly with Q^2 and x as expected, and are steeply falling with p_T and with a rise in the central region for η. In general terms, the distributions produced by the simulation are in good agreement with those from data. The predictions from CDM with $\lambda_s = 0.286$ for almost all the bins for all variables, overestimate the differential cross-sections. On the contrary, predictions by MEPS with $\lambda_s = 0.22$ are underestimate the amounts. The other two models are close to the measured values. The

74

ratio between MC models and data distributions show that the CDM model favours the strangness supression factor 0.22, while the MEPS model favours $\lambda_s = 0.286$.

The production of the Λ baryons is also investigated in Breit frame as a function of the transverse momentum p_T^{BF} and the momentum fraction x_p^{BF} in the target and current hemisphere separately. These are shown in figure (7.13). The production of strangeness due to hard interactions is expected to populate the current region. In the current hemisphere for p_T^{BF} both models, CDM and MEPS provide a good description in shape, and only for the last two bins their predictions are spread with respect to the measurement. In the target hemisphere, the predictions provided by CDM model with both values of the strangeness supression factor are slightly better than the MEPS model. With respect to the momentum fraction x_p^{BF} it is observed that MC models describe the behaviour of the differential cross-sections measured in both hemispheres. However, from the MC/data ratio we may observe that at high x_p in the current region MEPS model provides a better description than CDM model.
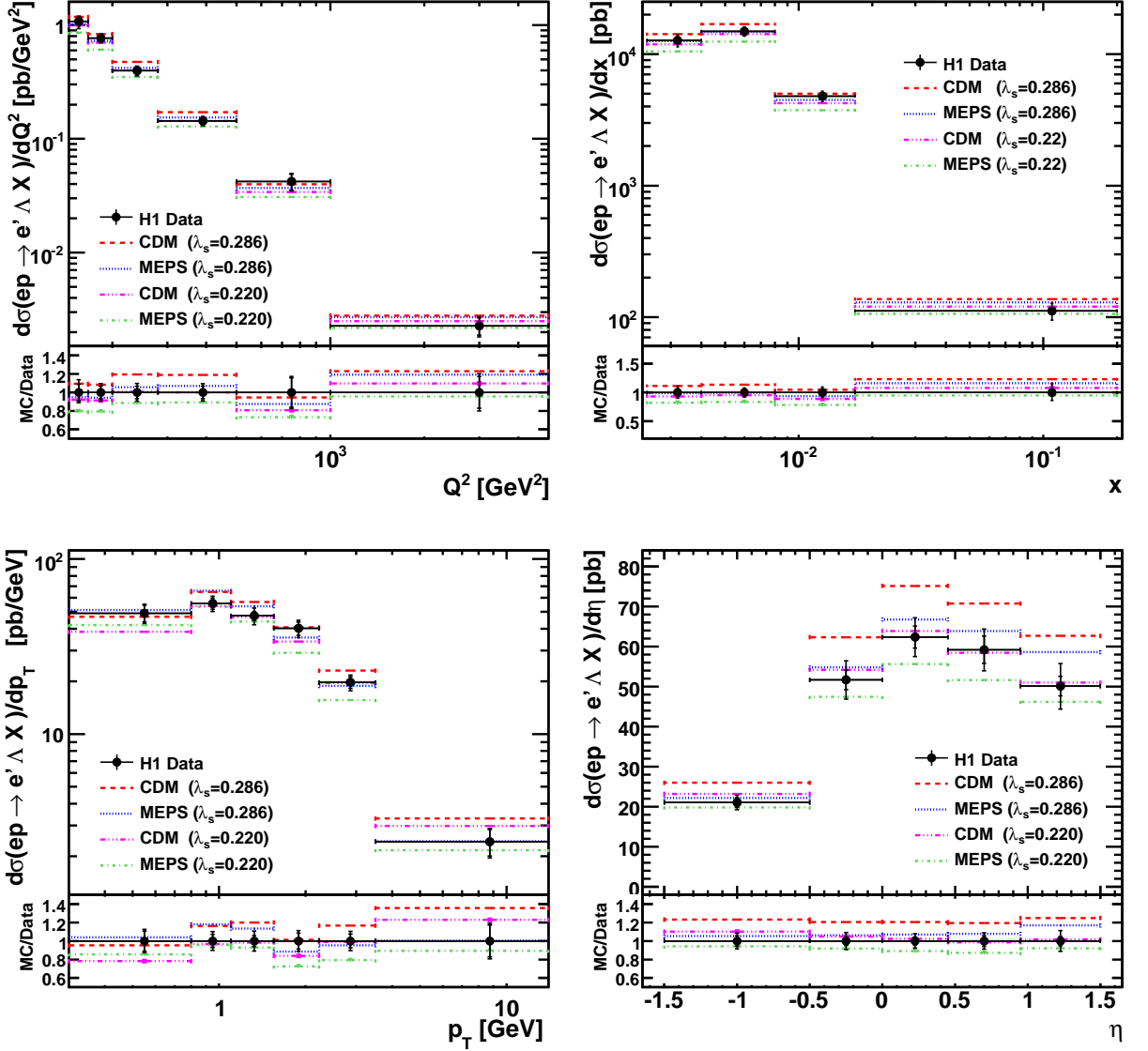
Figure 7.12: The differential cross sections for $[\Lambda + \overline{\Lambda}]$ in laboratory frame as a function of the event variables: photon virtuality squared Q^2, the Bjorken variable x. And kinematical variables: the transverse momentum p_T and the pseudorapidity η. The error bars show the total (outer) and statistical (inner) errors. On the bottom of each plot, the ratio $MC/Data$ are append for the prediction of the different MC models.
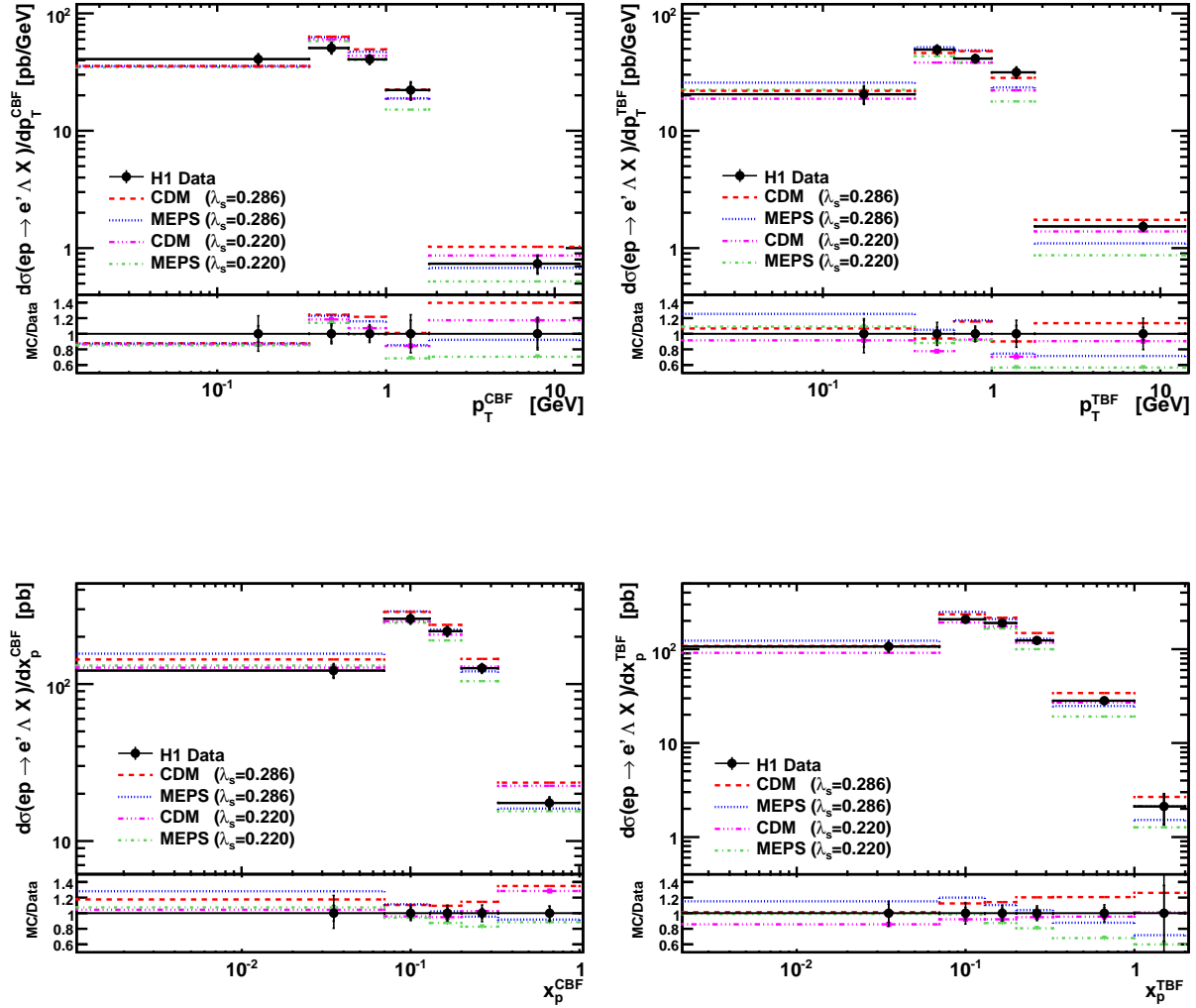
Figure 7.13: The differential cross sections for $[\Lambda + \overline{\Lambda}]$ in Breit frame as a function of the transverse momentum p_T^{BF} and the momentum fraction x_p^{BF} in the target (right column) and current (left column) hemisphere separately. The error bars show the total (outer) and statistical (inner) errors. On the bottom of each plot, the ratio $MC/Data$ are append for the prediction of the different MC models.

7.3 Asymmetry

Due to the nature of the colliding beams at HERA, the baryon number (BN) is equal to one in the final hadronic state, as iherited from by the proton beam. Measuring the asymmetry of production between baryon and antibaryon, gives us the possibility of understanding the mechanism of the BN transfer from the initial proton to a final baryon. There are studies in fixed target experiments that show that the influence of the source particle in the final hadron production is manifest in the forward region, as mentioned in [46].

The Λ and $\overline{\Lambda}$ production asymmetry measured in the present work may give us a hint if the initial proton has an influence in the Λ production. This because Λ^0 ($\overline{\Lambda}$) has uds ($\overline{u}\overline{d}\overline{s}$) valence quarks, and p has uud valence quarks, then Λ and p share two valence quarks which may be crucial to inherit the baryon number and favour an asymmetry.

The baryon-antibaryon asymmetry for Λ production is defined as

$$A_\Lambda = \frac{\sigma_{vis}(ep \to e\Lambda X) - \sigma_{vis}(ep \to e\overline{\Lambda}X)}{\sigma_{vis}(ep \to e\Lambda X) + \sigma_{vis}(ep \to e\overline{\Lambda}X)} \tag{7.26}$$

where $\sigma_{vis}(ep \to e\Lambda X)$ and $\sigma_{vis}(ep \to e\overline{\Lambda}X)$ are the cross sections obtained for Λ and $\overline{\Lambda}$ independently. A significant asymmetry may suggest a substantial transfer of baryon number from the the proton beam to the srange particle production. Taking the reported values for inclusive cross section in equations (7.20) and (7.21), the asymmetry obtained is,

$$\mathcal{A} = -0.002 \pm 0.022 \text{ (stat)} \begin{pmatrix} +0.018 \\ -0.018 \end{pmatrix} \text{ (sys)}. \tag{7.27}$$

This result is consistent with zero within erors. The theoretical predictions from the different MC models used in the present work are presented in Table (7.5).

The resulting asymmetry distributions for laboratory and Breit frames of reference respectively are presented in figures (7.14) and (7.14). All distributions lead to the same conclusion that there is no $\Lambda - \overline{\Lambda}$ asymmetry observed. The MC models arrive to the same conclusion. This indicates that the assumed proton influence on asymmetry is negligibly. These suggest that Λ baryon and its anti-particle are produced according to the same mechanism.

	CDM	MEPS
$\lambda_s = 0.220$	0.007 ± 0.005	0.013 ± 0.005
$\lambda_s = 0.286$	0.007 ± 0.004	0.013 ± 0.004

Table 7.5: MC predictions for the baryon-antibaryon asymmetry production.
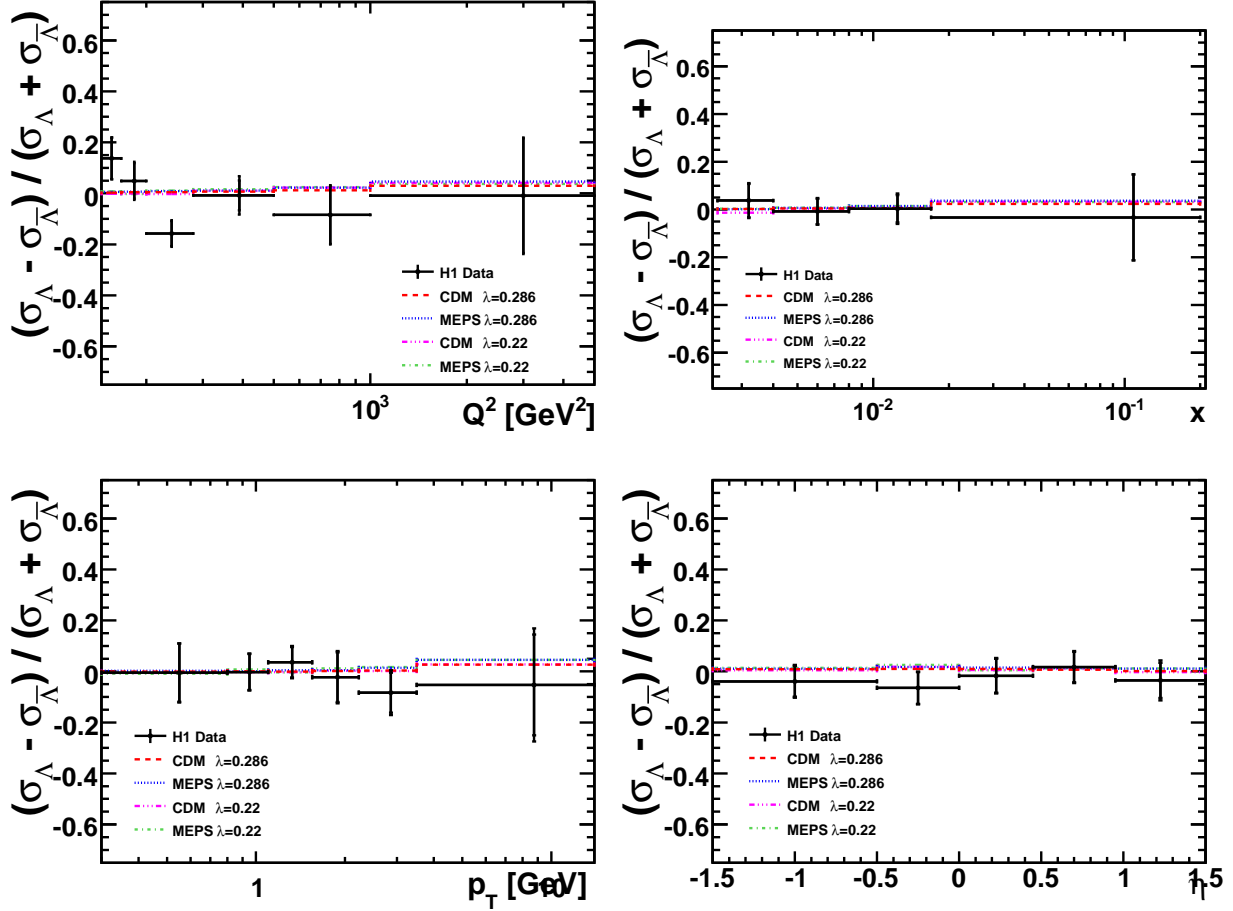
Figure 7.14: The asymmetry distribution $\mathcal{A}$ of the differential production cross-section in the laboratory frame as a function of the event variables: photon virtuality squared Q^2, the Bjorken variable x. And kinematical variables: the transverse momentum p_T and the pseudorapidity η. The error bars show the total (outer) and statistical (inner) errors.
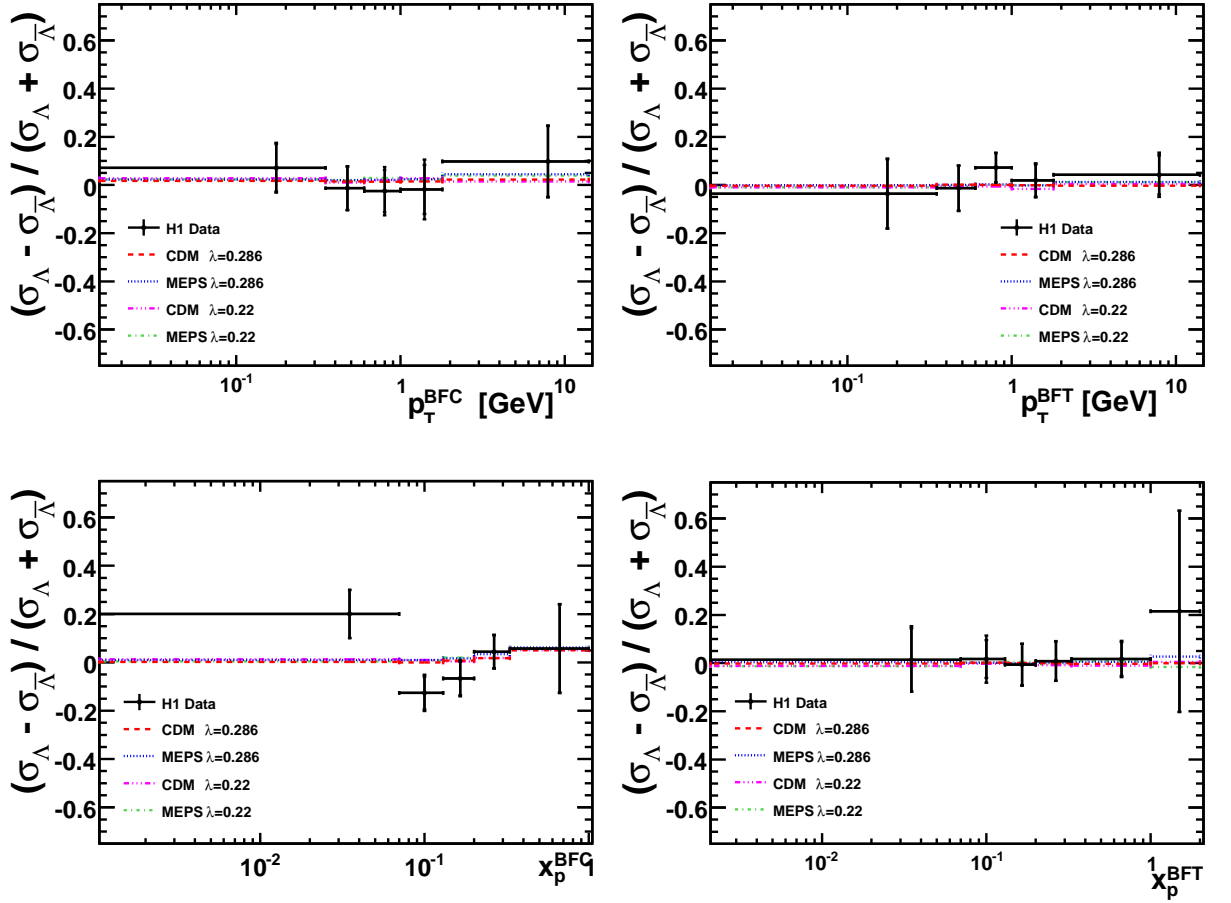
Figure 7.15: The asymmetry distribution $\mathcal{A}$ of the differential production cross-section in Breit frame as a function of the transverse momentum p_T^{BF} and the momentum fraction x_p^{BF} in the target (right column) and current (left column) hemisphere separately. The error bars show the total (outer) and statistical (inner) errors.

Bibliography

[1] I.S.Huges, *Elementary Particles*, Cambridge University Press. Third Edition, 1991.

[2] W.Hofmann, *Production of strange particles in hadronization process*, Nucl.Phys.A **479**:337c, 1988.

[3] Oxford University Department, *Deep inelastic scattering*, http://www.physics.ox.ac.uk/documents/PUS/dis/DIS.htm, 2003.

[4] Richard P. Feymann, *Very High Energy Collisions of Hadrons*, Phys.Rev.Lett. **23**:1415, 1969.

[5] J.D. Bjorken and E.A. Paschos, *Inelastic Electron-Proton and γ-Proton Scattering and the Structure of the Nucleon*, Phys.Rev. **185**:1975, 1969.

[6] F. Halzen and Alan D. Martin, Quarks and Leptons: *An Introductory Course in Modern Particle Physics*, New York,USA: Wiley(1984) 396p.

[7] V.D.Hopper and S.Biwas, *Evidence Concerning the Existence of the New Unstable Elementary Neutral Particle*, Phys.Rev. **80**:1099,1950.

[8] W.M.Yao *et al.*,[Particle Data Group], *Review of particle physics*, J.Phys.G **33**(2006), also available at http://pdg.lbl.gov

[9] N. Brook, *Momentum Spectra in the Current Region of the Breit Frame in Deep Inelastic Scattering at HERA*, J. Phys. G **25**:1445,1999.

[10] G. Thompson, N.A. McCubbin, J.V. Morris and D.P.C. Sankey, *Jet Findig in the Breit Frame*, J. Phys. G:Nucl.Part.Phys. **19**:1575,1993.

[11] V. Shekelyan, *Simulation and reconstruction in H1 Liquid Argon Calorimetry*, Internal Report. **H1-IN-288**,04/1993.

[12] K.Charchula,G.A.Schuler,H.Spiesberger *Combined QED and QCD radiative effects in deep inelastic lepton-proton scattering: Monte Carlo generator DJANGOH6*, Comput.Phys.Commun. **81**:381,1994.

[13] L.Lönnblad, *Parton Fragmentation and String Dynamics*, Comput.Phys.Commun. **71**:15,1992.

[14] L.Lönnblad, *ThePEG, PYTHIA7 and ARIADNE*, Proceedings of the DIS 2004 Workshop, Strbske Pleso, Slovakia.

[15] L.Lönnblad, *The Colour-Dipole model and ARIADNE program at High Q^2* , Proceedings of the Workshop on Monte Carlo generators fro HERA physics, DESY-PROC-1999-02 (1988/99).

[16] H.Jung *Hard diffractive scattering in high energy ep collisions and Monte Carlo Generator RAPGAP*, Comput.Phys.Commun. **86**:147,1995.

[17] J.Pumplin *et al.*, *New Generation of Parton Distribution with Uncertainties from Global QCD Analysis*, JHEP **0207** (2002). arXiv:hep-ph/0201195.

[18] B.Andersson, G.Gustafson, G.Ingelman and T.Sjöstrand, *Parton Fragmentation and String Dynamics*, Phys.Rept. **97**:31,1983.

[19] T.Sjöstrand, *High-energy-physics event generator with PYTHYA 5.7 and JETSET 7.4*, Comput.Phys.Commun. **82**:74,1994.

[20] A.Kwiatkowski *et al.* , *HERACLES: an event generator for ep interactions at HERA energies including radiative process*, Comput.Phys.Commun. **69**:155,1992.

[21] J.R.Gonçalo, *Simulation of the Hadronic final state and systematic uncertainties in high-Q^2 NC DIS*, ZEUS note, ZEUS-Note 02-004(2002).

[22] R.Barate *et al.* [ALEPH Collaboration], *Studies of Quantum Chromodynamics with ALEPH detector*, Phys.Rept. **294**:1,1998.

[23] G.A.Voss and B.H.Wiik, *The Electron Proton Collider HERA*, An.Rev.Nucl.Part.Sci. **44**:413,1994.

[24] I.Abt *et al.* [H1 Collaboration], *The H1 detector at HERA*, Nucl.Instrum.Meth.A **386**:310,1997.

[25] I.Abt *et al.* [H1 Collaboration], *The Tracking Calorimeter and Muon Detectors of the H1 experiment at HERA*, Nucl.Instrum.Meth.A **386**:310,1997.

[26] D.Pitzl et al., *The H1 silicon vertex detector*, Nucl.Instrum.Meth.A **454**:334-349,2000.

[27] W.Flauger, *Liquid Argon Calormetry at the H1 experiment*, Nucl.Instrum.Meth.A **289**:446-448,1990.

[28] C.Beigbeder, *Level 2 Topological Trigger (L2TT) Hardware*, H1-Internal Note, **H1-07**:98-547,1998.

[29] J.K.Kohne *et al.*, *Realization of a Second Level Neural Network Trigger for the H1Experiment at HERA*, Nucl.Instrum.Meth., **A389**:128-133,1997.

[30] E. Barrelet *et al.*, *The Hardware Implementation of L3 Triggers in H1*, H1-Internal Note, **H1-09**:88-100,1988.

[31] A.Baird *et al.*, *A Fast High Resolution Track Trigger for the H1 Experiment*, IEEE Trans.Nucl.Sci, **48**:1276-1285,2001.

[32] Marc A. Del Degan, *Spectroscopy in ep Scattering at HERA*, PhD thesis, Swiss Federal Institute of Technology Zurich, 2008.

[33] Denis Sunar, *Measurement of $K^{*\pm}(892)$ Production in Deep Ielastic ep Scattering with the H1 Detector at HERA*, PhD thesis, Universiteit Antwerpen, 2009.

[34] N.E.Berger, *A Measurement of Difractive ϕ Meson Photoproduction at HERA with the H1 Fast Track Trigger*, PhD thesis, Swiss Federal Institute of Technology Zurich, 2007.

[35] C.Kleinwort, *Energy Loss Measurement with the H1 Central Jet Chamber*, H1 internal note H1-IN-630(03/2008).

[36] J.Gassner, *A Measurement of D-Meson Production at HERA by Decay Vertex Identification*, PhD thesis, Swiss Federal Institute of Technology Zurich, 2002.

[37] V.Lubimov, *Particle separation by Lielihood Analysis of dE/dx Measurements in H1 Track Chambers*, H1 internal note H1-IN-329(11/1993).

[38] GEANT, *Detector Description and Simulation Tool*, CERN Program Library Long Writeup W5013, PHYS333.

[39] Rainer Wallny, *A Measurement of the Gluon Distribution in the Proton and of the Strong Coupling Constant α_s from Inclusive Deep-Inelastic Scattering*, PhD thesis, Zurich University, 2001.

[40] A.Blondel, F.Jacquet, *Measurements of Neutral and Charged Current Cross-Section in Electron-Proton Collisions at High Q^2 at HERA*,Proceedings of study of an ep facility for Europe, Ed. U.Amaldi. 1979.

[41] U.Bassler and G.Bernardi, *Proceedings of study of an ep facility for Europe*, Ed. U.Amaldi. DESY**79/48**:391-394,1979.

[42] Shiraz Habib, *Unpolarized Neutral Current $e^{\pm}p$ Cross Section Measurements at the H1 Experment, HERA*, PhD thesis, Universität Hamburg, 2009.

[43] C.Veelken, *H1NonepBgFinder - Rejection of Cosmic Muon and Beam-Halo Events in the H100 Framework*, H1 internal note H1-IN-603(09/2002).

[44] Lee West, *How to use the Heavy Flavour Working Group Track, Muon and Electron Selection Code*, H1 internal software manual (1997).

[45] F.D.Aaron *et al.* [H1 Collaboration], *Determination of the integrated Luminosity at HERA using Eleastic QED Compton Events*, Eur.Phys.J.C **72**:2163,2012.

[46] E.M.Aitala *et al.* [E791 Collaboration], *Asymmetries in the production of lambda zero, cascade minus and omega minus hyperons in 500 GeV/c pi minus-Nucleon Interactions*, Phys.Lett.B. **496**:9,2000.

[47] C.Liu, *Neutral Strangeness Production with ZEUS Detector at HERA*, PhD thesis, McGill University, Montreal,QC Canada 2007.

[48] A.C.Cottrell, *Strangeness Particle Production at the ZEUS Detector*, PhD thesis, University of Oxford 2005.

[49] B.Kopeliovich and B. Povh, *Baryon Asymmetry of the Proton Sea at Low x*, Zeit.Phys.C **75**:693,1997.